

5 Photoinjector

Synopsis

The front-end injection systems of the FERMI@Elettra linac produce the high brightness electron beams that define the performance of the FEL and the quality of the x-ray beams delivered to the users. The injector mainly consists of the RF gun, based on the BNL/UCLA 1.6 cell design [1] and scaled to European S-band frequency, its compensation solenoid and two traveling wave S-band rf sections (called SØA and SØB) which accelerate the beam up to 100 MeV. The slice emittance at the end of the injector is specified to be less than 1.5 mm mrad. The injector must provide a linearly current ramped bunch in order to linearize wakefield effects in the linac sections [2]. This requirement translates into finding the best laser pulse shape at the cathode that produces an electron bunch evolving into the desired current profile along the drift between the gun and the first booster section. Two main bunch configuration have been studied: a 0.8 nC/9 ps long “medium length bunch (MLB)” configuration and a 1 nC/11 ps “long bunch (LB)”. It is shown that the optimum laser temporal profile for both the MLB and the LB regimes is a quadratic ramp, which is transformed to a linear ramp by space charge forces in the injector. As the charge density varies from head-to-tail in the bunch, a best compromise has to be found for the emittance compensation process. As a consequence it is shown that slice emittance as well as charge distribution must be ramped along the bunch (see Paragraph 5.6.1): slice emittance values range from 0.7 to 1.1 mm mrad for the MLB regime and from 0.8 to 1.2 mm mrad for the LB regime while the current increases from 40 A up to 80 A.

Furthermore, since a seeded harmonic cascade FEL is very sensitive to shot-by-shot variations in beam characteristics, the effects of jitters on the FEL performance have been studied in the ramped current scenario. In particular, time jitters are critical because they are translated into energy jitter in the two

chicanes, thus affecting the FEL output power stability. The main source of time jitter comes from jitter in the drive laser arrival time at the cathode with respect to the gun RF waveform, specified to be equal to or less than 200 fs and corresponding to a 0.1 deg jitter in the RF phase seen by the beam. Hundreds of simulation of the injector output beam quality (Section 5.6.2) with input parameters randomly picked, within tolerance values dictated by present technology and supported by measurements, have been performed; they show that the overall expected rms time jitter value at the injector exit is 350 fs. Sensitivity studies and tolerance budgets concerning injector output current, energy, emittance and injector optics parameters are included in the discussion.

5.1 Introduction

This chapter describes the critical technical components of the photo-injector system and the associated beam dynamics, optimized to deliver the high quality electron beams FERMI requires.

Section 5.2 provides an overview of the various injector systems and subsystems. Different injector operating modes are described corresponding to the different linac set-up's required by FEL beam characteristics tailored to meet user needs.

Sections 5.3 and 5.4 describe the main photoinjector components: electron source and RF gun. The photoinjector drive laser main specifications are given at the end of Section 5.3 and discussed in more detail in Chapter 10.

RF gun design considerations are presented in Section 5.4, where various cavity geometry options, studied in order to optimize the efficiency of energy transfer to the electron beam, are described. A study of power coupling into the various cavity modes falling within the bandwidth of the RF drive pulse is also presented, followed by a study of the transient cavity response and, finally, of the effects of the cavity design on the extracted beam quality.

Section 5.5 describes the low energy, off-axis diagnostics beamline. Beam dynamics simulation results using ASTRA, GPT, ELEGANT, and MAD are presented.

Section 5.6 beam dynamics optimization studies are discussed for the various operating modes. Optimized baseline beamline configurations and drive laser pulse shapes are presented, supported by space-charge tracking codes simulations. Optimization of the beam transport through the linac sections up to the FEL undulator entrance requires significant deviations from the canonical 'flat-top' temporal laser pulse shape at the photocathode. The physics of nonlinear electron current emission has been revisited in order to find the optimum temporal profile of the drive laser. It is shown that a linear current ramp at the injector output is required and that the laser pulse intensity should therefore follow a quadratic curve. Parametric sensitivity studies are performed around the baseline configurations and jitter studies are presented showing the stability degree of the found solutions. The conclusions of this chapter are summarized in Section 5.7.

5.2 Overview of Electron Source and Injection System

The front-end injection system of the FERMI linac is designed to produce the high brightness electron beams that determine the FEL performance and the quality of x-ray beams delivered to the users. The electron source and the injection system are specifically designed to minimize technical risk and

cost by utilizing existing accelerator components and by leveraging on the technical designs of other, contemporary x-ray FEL projects. The injector major components are shown in Figure 5.2.1.

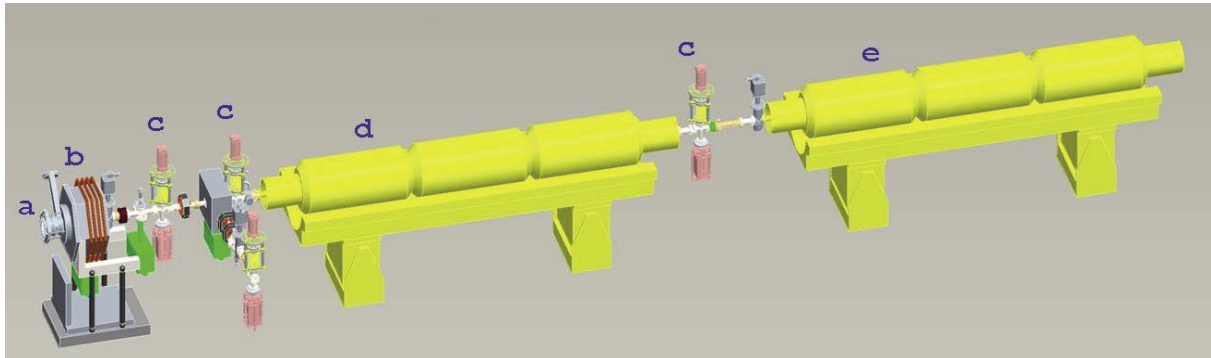


Figure 5.2.1:
The FERMI@Elettra FEL photoinjector.
a) RF Gun, b) Solenoid,
c) Pop-in screens, d), e) SØA and SØB
booster accelerating sections.

5.2.1 Electron Source and RF Gun

The FERMI electron source is a metallic photocathode (polycrystalline copper) illuminated by an intense, 263 nm wavelength UV laser whose pulse shape is chosen to optimize the final beam quality. Because the best measured values of the quantum efficiency of copper at 263 nm are in the range 10^{-5} - 10^{-4} , the laser must deliver $\sim 500 \mu\text{J}$ on the cathode in order to produce a $\sim 1 \text{ nC}$ bunch charge.

The photocathode also serves as the conducting back plane of a one and a half cell RF gun. A first stage gun is designed for a pulse repetition rate of up to 10 Hz. An upgraded version, not described here, reaching up to 50 Hz repetition rate, is foreseen as a second stage.

The first stage gun operates in the fundamental, TM_{010} - π ('pi') mode of the two-cell cavity, resonant at 2997.9 MHz. Its design utilizes, with appropriate slight shape modifications, proven industrialized technologies, previously optimized for operation at 2856 MHz.

It is specified to provide a peak accelerating gradient of 110 MV/m, and an output beam energy of $\sim 5 \text{ MeV}$ at 10 Hz repetition frequency. It is powered by a fraction ($\sim 60\%$) of the power delivered by the first linac klystron. The cavity filling time to its nominal field value is $\sim 2.8 \mu\text{sec}$ assuming a 10 MW peak input pulse.

External solenoid magnets are integral to the RF gun operation. A multiple pancake, emittance compensating solenoid provides focusing to help transport the beam from the gun exit to the entrance of the booster linac structures.

5.2.2 Gun-to-Linac Drift

The gun-to-linac (GTL) drift section encompasses the beamline from the gun exit to the entrance of the first booster accelerator (see Figure 5.2.2).

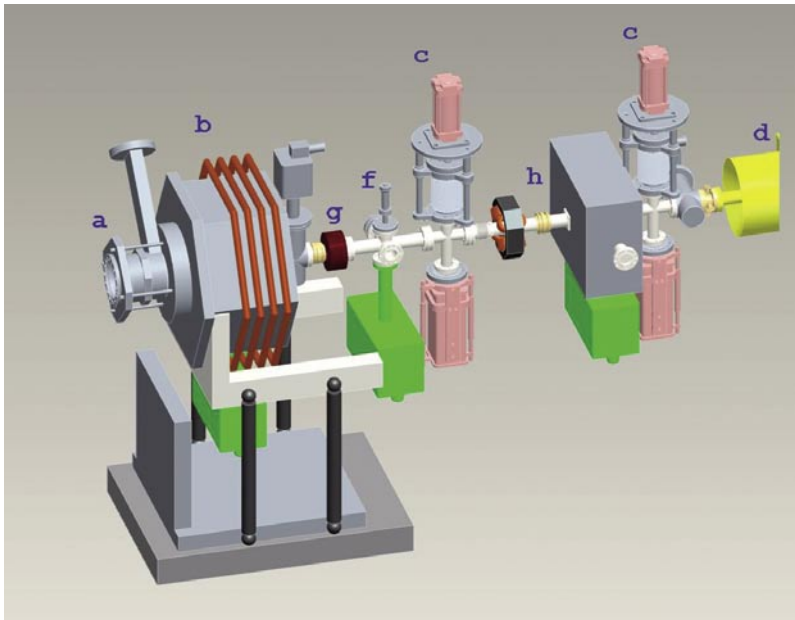


Figure 5.2.2:
Gun-to-linac beamline. See text for details.

The GTL beamline contains the instrumentation for the low energy beam diagnostics and trajectory correction, and the vacuum instrumentation for the entire front-end section. Two dipole trim magnets (h) allow correcting beam offset and angle. Two vacuum crosses (c) support retractable beam profile image screens, a charge-measuring Faraday cup and horizontal and/or vertical slits. An inductive toroid (g) is placed near the gun exit for non-destructive bunch charge measurements. A six-way cross (f) in the beamline allows for on-axis injection of the photocathode drive laser pulse, vacuum pumping and measurement.

Together with the low energy, off-axis diagnostic beamline, the GTL allows measuring transverse and longitudinal beam phase space properties.

5.2.3 Low Energy Diagnostic Beamline

The off-axis, low energy diagnostic beamline concept is shown in Figure 5.2.3. It is equipped with a magnetic spectrometer to measure beam energy and energy spread, an important tool for optimizing the gun performance.

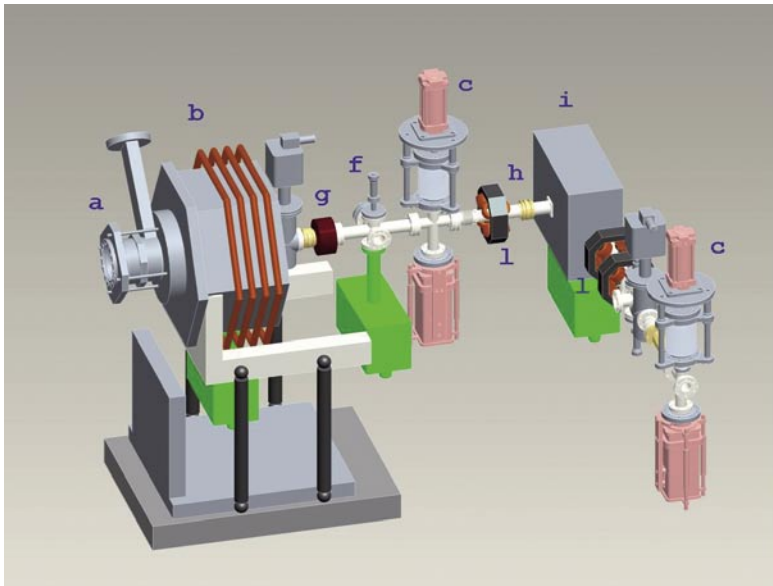


Figure 5.2.3:
Off-axis, diagnostic beamline. See text for details.

The beamline main components are: the 90-degree spectrometer magnet (i), three quadrupole magnets (l), two dipole trim magnets, a beam profile screen and a Faraday cup (c). The beamline dispersion is adjusted so as to maximize the spectrometer energy resolution.

5.2.4 Booster Accelerating Modules

The two booster traveling-wave accelerating structures SØA and SØB, are shown in Figure 5.2.1. Each section is composed of 93 identical on-axis, iris-coupled cells, resonating at 2.998 GHz. The two end cells are used to couple RF power into and out of the structure. The ~ 3.3 m active structure length requires ~ 3.5 m of beamline. It operates in the $2\pi/3$ mode, and provides peak accelerating gradients of ~ 19 MV/m, for a total maximum energy gain of ~ 45 MeV (including a 10% margin). The booster sections are equipped with solenoids to provide transverse focusing, to assist with emittance compensation, and to match the optical (lattice) functions at the input to the main linac.

5.2.5 Operating Modes

Several configurations of the electron bunch to be produced have been considered in the optimization study process, in order to make the machine design as flexible as possible so as to satisfy the various user requirements [3]. Eventually, two main bunch configurations have been selected: a “medium length bunch (MLB)” configuration and a “long bunch (LB)” one. At the linac output the bunch design specifications call for a 600 fs/1 kA peak in the MLB mode and a 1.5 ps /0.5 kA peak in the LB mode.

The simulations of e-beam dynamics have been separated into two parts: tracking through the low energy injector part, including SØA and SØB, in which the beam is space charge dominated (up ~ 100 MeV), and tracking through the rest of the linac. Injector simulations are performed using two space charge tracking codes: ASTRA [4] and GPT [5].

As discussed in Chapter 6, in order to compensate the wakefield effects in the linac sections and to provide a flat distribution in phase space at the linac output, the injector output electron bunch current distribution is designed to be linearly ramped in time [6], in both the MLB and the LB regimes. This unconventional specification originated in the Linac optimization studies, which showed that the nonlinearity of the linac accelerating field waveform and the nonlinear time-of-flights in the bunch compressors play an important role in beam dynamics [2,6] and are such that, with the commonly used flat top charge distribution, the longitudinal phase space footprint at the end of the linac would exhibit a quadratic chirp degrading the FEL performance [7].

5.3 Photocathode and Drive Laser Systems

The photoinjector system for FERMI requires a robust, pulsed UV laser system. The system requirements for the photoinjector laser are presented in Table 5.3.1.

Table 5.3.1: Temporal specifications for the UV laser pulse.

Wavelength	< 270 nm
Required pulse energy at the cathode (Cu)	~0.5 mJ
Pulse duration range (FWHM)	1 - 20 ps
Rise/fall time range (10-90 %)	0.5 - 5 ps
Instantaneous power flatness (rms)	< 5%
Synchronization (rms)	< 300 fs
Pulse repetition rate range	10 Hz - 50 Hz

Specifications for the beam transverse profile parameters at the cathode are listed in Table 5.3.2:

Table 5.3.2: Spatial specifications for the UV laser spot at the photocathode.

Beam diameter range (FWHM)	2-4 mm
Edge ramp width (10-90 %)	0.5 mm
Intensity flatness (rms)	< 5%

Beam shaping techniques based on refractive, reflective, diffractive, and absorptive optics are used to transform Gaussian-like spatial profiles into the desired longitudinal profile [8]. A more detailed description of the photoinjector drive laser is given in Chapter 10.

5.4 RF Gun Design and Optimization

Meeting the FERMI photoinjector electron beam brightness specifications requires studying all possible perturbation effects in the RF gun that may degrade the beam quality. The present generation of RF guns allows a coupled-cavity, resonant ‘zero’ order mode, at a frequency lower (typically by ~ 10 MHz) than that of the main accelerating mode (the ‘pi’ mode), and that can be excited by the drive klystron pulse. Its undesired field may rise to significant amplitude and thus interfere with the beam dynamics of the emitted electrons, eventually affecting the beam quality. To evaluate such effects, the frequency separation between the two resonant modes was studied for different cavity geometries. The coupling between the gun cavity and the power feed wave guide has also been analyzed, together with the transient effects during cavity filling. After estimating the amplitude of the excited ‘zero’ mode, beam dynamics simulations were performed showing the beam quality behavior as a function of the zero mode amplitude and frequency separation.

5.4.1 RF Cavity Design

The first gun cavity design [9] was obtained by reducing the BNL/SLAC/UCLA 1.6 gun geometry by a factor $K = f_{BNL}/f_{FERMI} \approx 0.96$. Such simple scaling does raise the main resonant frequency from 2856 MHz to 2997.9 MHz, but disregards other issues involved in normal conducting RF cavity optimization [10]. In particular, to investigate ways of increasing the resonant frequency separation between the pi and the zero modes and to decrease the coupling of the zero mode to the klystron drive pulse, several RF cavity geometries have been examined, all resonating at the European frequency of 2997.9 MHz but differing in cell lengths and pi-to-zero mode frequency separation. A detailed study of the cavity

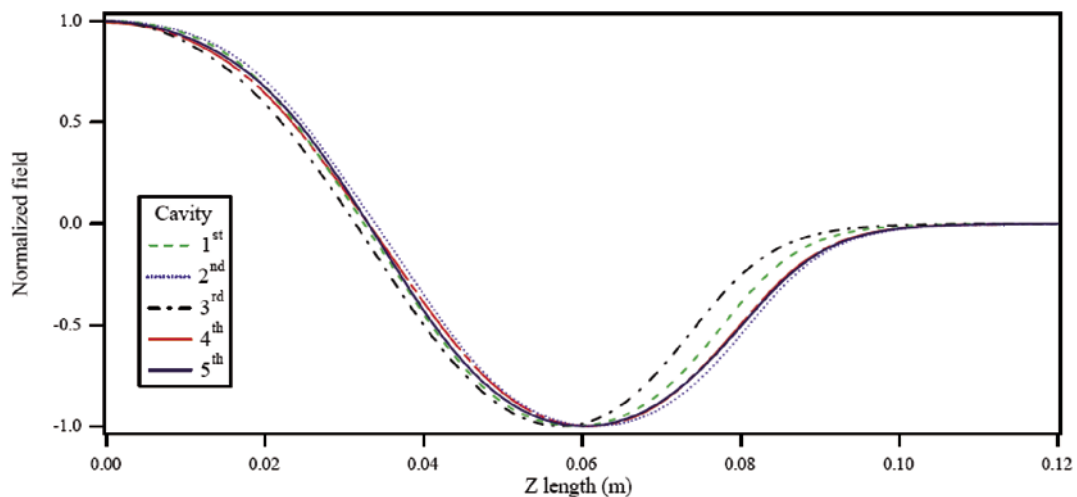


Figure 5.4.1:
Axial electric field of the five cavities (pi-mode).

modes was performed using both frequency-domain and time-domain electromagnetic models [3]. For the largest foreseeable separation, the cavity drive efficiency decreases by $\sim 10\%$. Great care was taken, using SUPERFISH modeling, to re-scale and optimize each cavity geometry to produce a nearly 1:1 ratio between the pi-mode peak field in the full and in the half cells, as well as to control the frequency separation between the two resonant modes. Various geometries are described in detail in [3, 11].

Field profiles along the axis, for 5 such cases, whose parameters differ slightly while all falling within an acceptable range, are shown in Figure 5.4.1. The main difference between cases is the value of the launching phase that optimizes the beam energy gain and plays an important role in the beam dynamics.

Ref. [3] describes in detail the dependence of shunt impedance on the cavity geometry and the calculations of the effective R/Q for all design options.

5.4.2 Power Coupling

In order to estimate the power coupling between the gun and the waveguide, a three-dimensional model of the basic pillbox RF gun structure was created and implemented using Microwave Studio [12] (Figure 5.4.2). The results obtained are in good agreement with SUPERFISH models. The cavity is modeled with symmetric waveguides and ports. Full height WR-284 waveguides are used: they extend to within 3 mm from the outer cavity walls, in which a rectangular opening provides the waveguide-to-cavity coupling iris. The dimensions of the coupling aperture were varied until the time-domain response, at the smallest mode frequency separation, roughly corresponded to the values measured at the SLAC gun Test Facility (GTF) [13]. The coupling aperture dimensions were then kept fixed while adjusting the cells iris radius to vary the π and zero mode frequency separation. The frequency separation was also varied by varying cell geometries.

Time-domain calculations were also performed using Microwave Studio to obtain the waveguide coupling factors (β) for the pi and zero modes at their resonant frequencies. Results have shown that, in all cases studied, the pi mode is over-coupled ($\beta > 1$) while the zero mode is under-coupled ($\beta < 1$).

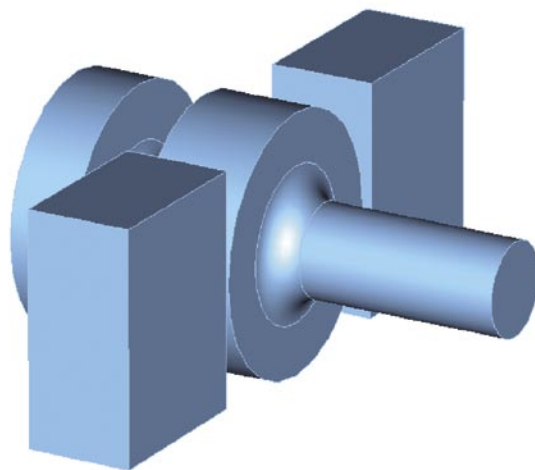


Figure 5.4.2:
Microwave Studio model for the RF gun with dual waveguide feeds.

5.4.3 Klystron Pulse Shape and Gun Cavity Transient Response

The transient response of the two-mode RF gun structure has been analyzed using a realistic excitation signals.

A model of the klystron pulse that drives the cavity modes, assumed to have a 3 μ sec flat-top with linear, 100 ns, rise and fall times and a superimposed single carrier frequency modulation at 2998 MHz, has been analyzed. The amplitude and the relative phase of the klystron pulse frequency components, normalized to the 2998 MHz component are plotted in Figure 5.4.3 versus their frequency difference from the 2998 MHz. The drive pulse amplitude ratio and relative phase with respect to the 2998 MHz component are tabulated in Table 5.4.1.

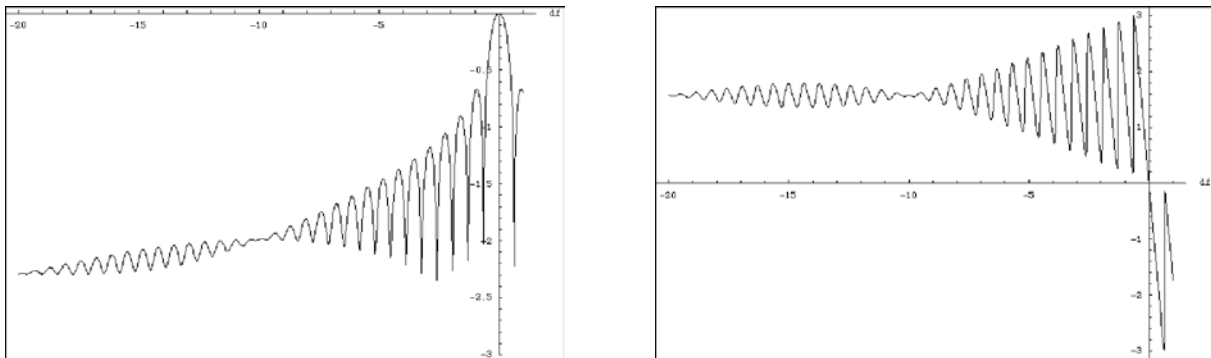


Figure 5.4.3:
Log-amplitude (left) and relative phase (right) of the klystron voltage pulse frequency components, normalized to the 2998 MHz component, versus frequency difference (in MHz).

At large offsets from the carrier frequency and at steady-state, the relative amplitude is seen to decrease exponentially, while the relative phase oscillates about $\pi/2$. Hence, one does expect that, at steady-state, while the π mode will track the phase and amplitude of the 2998 MHz component, the zero mode amplitude and phase will deviate from it as shown in Figure 5.4.3. This estimate does not account for differences in coupling to the klystron pulse for the two modes, nor for mode quality factor differences in coupling to the klystron pulse of the two modes, nor for mode quality factor differences. Those effects are discussed in the next sections.

Table 5.4.1: Relative amplitude and phase at several frequency offsets from the carrier frequency.

Δf (MHz)	0	-3.5	-5	-10	-15	-20
Relative amplitude	1.	0.052	0.024	0.010	0.007	0.005
Relative phase ($^\circ$)	0.	77.94	122.5	90.	102.0	90.

5.4.4 Two-Mode Resonant Cavity Response under Ideal RF Drive

The behavior of the RF gun structure under non-trivial RF drive waveforms is determined from analysis of the equivalent circuit equation. The transient and steady state response of the cavity modes have been determined and related to measured values of the fields in the full- and the half-cells. In this section, the RF drive waveform is assumed to take an idealized, though nontrivial form, the phase of the RF drive signal was assumed to remain constant over the pulse.

Assuming that the two cavity modes (0 and π) present within the bandwidth of the RF drive, are independently coupled (frequency separation between the two modes larger than the width of each resonance), the time dependence of the voltage of each mode with the coupling to finite conductivity walls and an external waveguide can be expressed as [3]:

$$\left(\frac{d^2}{dt^2} + \frac{\omega_0}{Q_{L,0}} \frac{d}{dt} + \omega_0^2 \right) V_0 = \frac{2n_0\omega_0}{Q_{ext,0}} \frac{d}{dt} V_{+,0} \quad 5.4.1$$

$$\left(\frac{d^2}{dt^2} + \frac{\omega_\pi}{Q_{L,\pi}} \frac{d}{dt} + \omega_\pi^2 \right) V_\pi = \frac{2n_\pi\omega_\pi}{Q_{ext,\pi}} \frac{d}{dt} V_{+,\pi} \quad 5.4.2$$

Under constant phase approximation, a time domain solution to equations 5.4-1 and 5.4-2 that allows an analytical formulation of both transient and steady-state behaviors has been derived [3]:

$$\begin{aligned} \tilde{V}_\pi(t) & \left(V_{F0} n_\pi \frac{2\beta_\pi}{1+\beta_\pi} \right) = \cos\psi_\pi e^{-i\psi_\pi} \times \\ & \left(\left\{ 1 - e^{-\left(\frac{1+i\tan\psi_\pi}{2Q_{L,\pi}}\right)\omega t} + (\omega\tau - i) \left[\frac{\omega\tau + 2Q_{L,\pi} \cos\psi_\pi e^{i\psi_\pi}}{(\omega\tau)^2 + (2Q_{L,\pi} \cos\psi_\pi)^2} \right] \left[e^{-\left(\frac{1+i\tan\psi_\pi}{2Q_{L,\pi}}\right)\omega t} - e^{-(\omega t)/(\omega\tau)} \right] \right\} - \right. \\ & \left. H(t-T) \left\{ 1 - e^{-\left(\frac{1+i\tan\psi_\pi}{2Q_{L,\pi}}\right)\omega(t-T)} + (\omega\tau - i) \left[\frac{\omega\tau + 2Q_{L,\pi} \cos\psi_\pi e^{i\psi_\pi}}{(\omega\tau)^2 + (2Q_{L,\pi} \cos\psi_\pi)^2} \right] \left[e^{-\left(\frac{1+i\tan\psi_\pi}{2Q_{L,\pi}}\right)\omega(t-T)} - e^{-\omega(t-T)/(\omega\tau)} \right] \right\} \right) \\ \tilde{V}_0(t) & \left(V_{F0} n_0 \frac{2\beta_0}{1+\beta_0} \right) = \cos\psi_0 e^{-i\psi_0} \times \\ & \left(\left\{ 1 - e^{-\left(\frac{1+i\tan\psi_0}{2Q_{L,0}}\right)\omega t} + (\omega\tau - i) \left[\frac{\omega\tau + 2Q_{L,0} \cos\psi_0 e^{i\psi_0}}{(\omega\tau)^2 + (2Q_{L,0} \cos\psi_0)^2} \right] \left[e^{-\left(\frac{1+i\tan\psi_0}{2Q_{L,0}}\right)\omega t} - e^{-(\omega t)/(\omega\tau)} \right] \right\} - \right. \\ & \left. H(t-T) \left\{ 1 - e^{-\left(\frac{1+i\tan\psi_0}{2Q_{L,0}}\right)\omega(t-T)} + (\omega\tau - i) \left[\frac{\omega\tau + 2Q_{L,0} \cos\psi_0 e^{i\psi_0}}{(\omega\tau)^2 + (2Q_{L,0} \cos\psi_0)^2} \right] \left[e^{-\left(\frac{1+i\tan\psi_0}{2Q_{L,0}}\right)\omega(t-T)} - e^{-\omega(t-T)/(\omega\tau)} \right] \right\} \right) \end{aligned} \quad 5.4.3$$

The equivalent circuit parameters are related to measured quantities: coupling, calibrations derived from numerical simulations, cavity shunt impedance and electric field at the cathode.

An ideal RF source waveform has been assumed, defined as:

$$V_F(t)/V_{F0} = H(t)(1 - e^{-t/\tau}) - H(t - T)(1 - e^{-(t-T)/\tau}) \quad 5.4.4$$

The rise and fall times of the waveform (τ) are assumed to be 100 ns, for a 10%-90% pulse risetime of ~220 ns. The pulse is held for 3 μ sec (T) before it begins to decay. The drive source central frequency is matched to that of the π mode in the cavity. The WR-284 waveguide cutoff frequency is 2.08 GHz for the dominant TE_{10} mode. The peak power of the forward wave is adjusted to produce ~110 MV/m at the cathode in the π mode.

A Python script was written to generate the time dependent complex mode voltages (Eq. 5.4-3) from the RF power source waveform (Eq. 5.4-4). For four different frequency separation cases (4.6 MHz, 7.12 MHz, 12.5 MHz, 17.6 MHz) the corresponding waveforms for the forward and reverse waves, the peak cathode electric field in the pi and zero modes, and the combined electric field in the half and full cavity cells have been calculated. The electric field was obtained from field measuring probes inserted in both cells and, in presence of a significant zero mode excitation they do differ significantly from the unperturbed pi mode values. Figure 5.4.4 displays, for the 12.5 MHz case, the forward and reverse wave amplitudes (a) and the peak pi and zero modes electric fields (b).

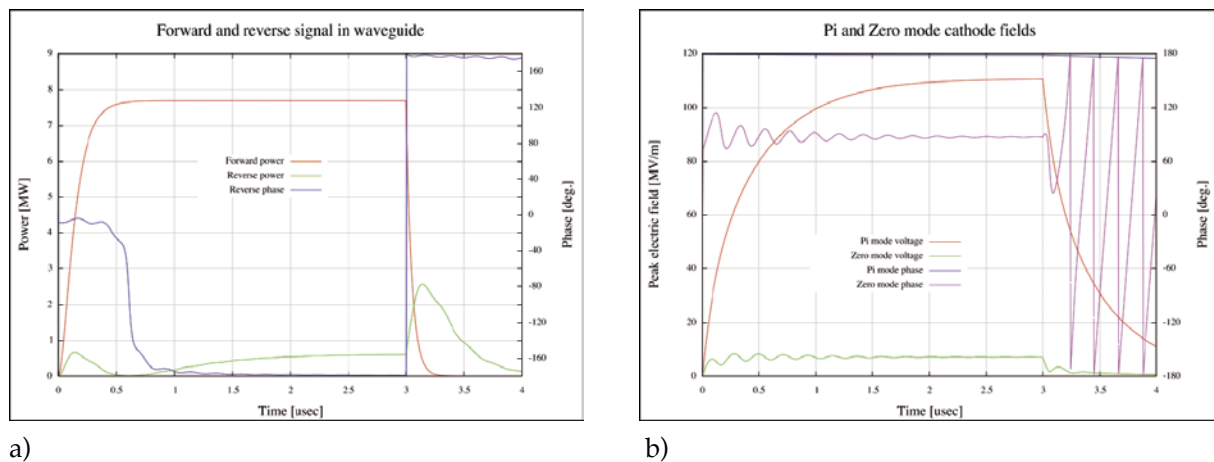


Figure 5.4.4:
Incident and observed waveforms for
12.5 MHz frequency separation.

Even though this model makes several assumptions, such as constant phase of the drive pulse throughout the entire pulse length, it provides an analytical, closed-form expression useful to predict the state of the fields in the RF gun cavities at any time during the pulse, in order to pursue beam dynamics studies, and against which measured quantities may be benchmarked.

5.4.5 Two-Mode Resonant Cavity Response under Measured or Simulated RF Drive

The behavior of the RF gun structure under non-trivial RF drive waveforms is derived from numerical analysis of the equivalent circuit equations. In order to benchmark the technique, the computed transient and steady-state cavity responses are compared to measured values of the fields in the full and half cells of the GTF RF gun.

The circuit equations in the time domain are solved by integrating the differential equations from Section 5.4.4 in the slowly varying envelopes approximation [3].

The complex RF drive voltage waveform is obtained by measuring the forward klystron pulse amplitude and phase at a power divider upstream of the RF gun full cell. The forward phase is measured with respect to a low-level clock signal. The same power divider, which also functions as a directional coupler, is used to measure the reflected signal.

In order to benchmark the results of the method against FERMI Linac measured data, the SLAC GTF injector case was simulated first, using a particular GTF measured waveform [14] as the drive pulse. The resulting forward wave signals were used to derive the complex voltage waveform driving the pi and zero modes, which can be written

$$\tilde{V}_+ = |\tilde{V}_+| e^{-i\varphi_+}, \quad 5.4.5$$

where amplitude and phase are both time dependent quantities. Under the slowly (with respect to the instantaneous phase of the drive signal) varying envelope approximation, the derivative of the complex waveform is expressible in terms of derivatives of the envelope amplitude and phase:

$$\tilde{V}'_+ = \left(|\tilde{V}'_+| - i\varphi'_+ |\tilde{V}_+| \right) e^{-i\varphi_+} \quad 5.4.6$$

Equations of motion 5.4-5 and 5.4-6 were numerically integrated using a Python script and the results of the fit are shown in Figure 5.4.5, displaying excellent agreement between the computed and measured waveforms. The mode frequency-beating in the cavity field amplitude is evident.

An analysis of the GTF injector case was first of all performed to benchmark the results of this method against the measured data. The results of the fit are shown in Figure 5.4.5, displaying excellent agreement between the calculated and measured waveforms. The mode frequency-beating in the cavity field amplitude is evident.

Applying this method to the FERMI FEL injector to four different frequency separation values yields the corresponding forward and reverse waveforms, the peak cathode electric fields in the pi and zero modes and the combined electric fields in both the half and the full cells. The latter quantities are measured by field probes in both cells. Input parameter values were computed using Superfish and the drive frequency was matched exactly to the pi mode resonance. In addition, only near-critical coupling of the waveguide to the RF gun, $\beta_\pi = \beta_0 = 1.05$, was assumed for both modes. For all four cases the results are

generally similar to the GTF ones quoted above and, as mentioned earlier, in presence of significant zero mode excitation the combined fields do differ significantly from the unperturbed pi mode values.

The peak forward power required to drive the peak pi mode amplitude to ~ 110 MV/m is empirically determined and the time along the pulse at which the peak amplitude is reached in the full-cell, which is the time at which the electron beam should be launched by firing the photocathode drive laser, is recorded. Peak electric field values and phases relative to the forward wave phase are tabulated in Table 5.4.2.

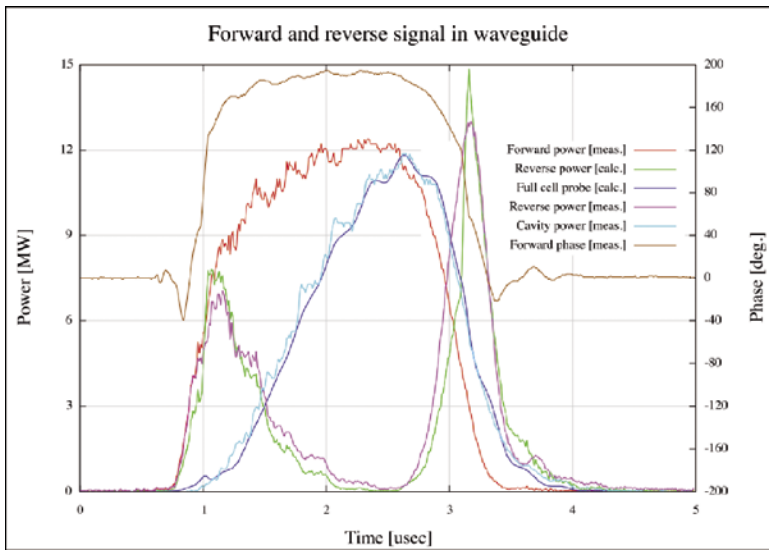


Figure 5.4.5: Measured and calculated time dependence of the forward and reflected power from the RF gun, and full cell cavity probe signal.

Table 5.4.2: FERMI RF gun operational parameters.

Mode separation, Δf [MHz]	4.6	7.12	12.5	17.6
P_{forward} [MW]	9.2	9.3	9.9	10.1
t_{peak} [μsec]	2.82	2.81	2.81	2.82
ϕ_{forward} [$^{\circ}$]	174.3	175.2	175.2	174.3
P_{cav} [MW]	7.05	7.1	7.5	7.6
E_{π} [MV/m]	110.3	109.9	110.2	110.4
$\Delta\phi_{\pi}$ [$^{\circ}$]	-6.7	-6.8	-6.8	-6.6
E_0 [MV/m]	9.07	5.86	3.1	2.4
$\Delta\phi_0$ [$^{\circ}$]	-92.4	-83.6	-83.2	-86.1
$\Delta\phi_0 - \Delta\phi_{\pi}$ [$^{\circ}$]	-85.7	-76.8	-76.4	-79.5
E_{half} [MV/m]	111.3	111.4	111.0	110.9
$\Delta\phi_{\text{half}}$ [$^{\circ}$]	-11.3	-9.8	-8.4	-7.8
E_{full} [MV/m]	110.	108.8	109.6	110.0
$\Delta\phi_{\text{full}}$ [$^{\circ}$]	178.1	176.2	174.8	174.6
$\Delta\phi_{\text{full}} - \Delta\phi_{\text{half}}$ [$^{\circ}$]	189.4	186.0	183.2	182.4

5.4.6 Beam Dynamics Simulations

The analysis of the previous section yields a data set describing the optimized cavity parameters at the appropriate electron beam launching time. The analysis has been used to perform parametric sensitivity studies and to generate accurate relative field and phase values for beam dynamics calculations.

The effect of zero-mode excitation on the beam dynamics has been studied for the MLB bunch case, assuming for simplicity a flat-top bunch profile [15]. Similar analyses can be extended to the ramped-current bunches. The electron beam was generated from a 9 ps (FWHM) long, flat topped drive laser pulse with 0.5 ps linear rise and fall times. The (hard edge) spot size diameter at the cathode was 1 mm. The bunch charge was 800 pC and the initial (thermal) emittance is ~ 0.6 mm mrad [16]. The evolution of the transverse rms beam phase space and of the emittance is shown in Figure 5.4.6. Slice parameters were computed using 1 ps length slices, symmetric about the bunch center-of-charge. The bunch longitudinal blow-up decreases the slice peak current from an initial value of ~ 90 A at generation to ~ 75 A at the booster linac entrance and all the way down to the injector exit.

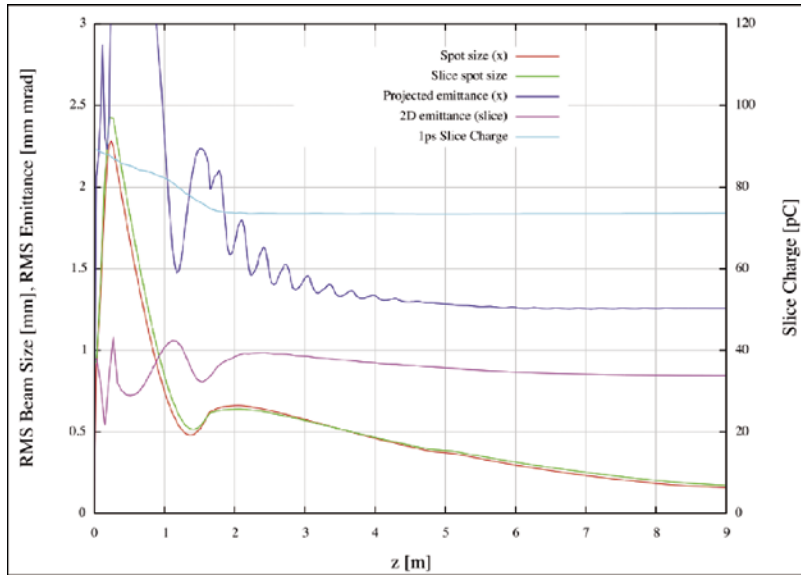


Figure 5.4.6:
Transverse beam evolution through the injector.

Figure 5.4.7 shows the beam energy and longitudinal emittance evolution in the injector. The average beam energy reaches ~ 95 MeV at the injector exit. The rms bunch length grows by $\sim 30\%$, from ~ 0.8 mm to ~ 1.05 mm. The region of largest longitudinal blow-up rate is the gun-to-linac drift space, where the beam has relatively low kinetic energy and is decreasing in spot size under the effect of emittance compensation processes and of matching to the linac optics.

The longitudinal emittance is defined as

$$\varepsilon_z = \sqrt{\langle z^2 \rangle \langle \Delta E^2 \rangle - \langle z \cdot \Delta E \rangle^2}, \quad 5.4.7$$

where z and ΔE are the particle offset in longitudinal position and the energy offset with respect to the synchronous particle. Figure 5.4.7 displays the evolution of longitudinal emittance, total rms energy spread and linear correlation of the longitudinal phase space $\langle z (d\Delta E/dz) \rangle$.

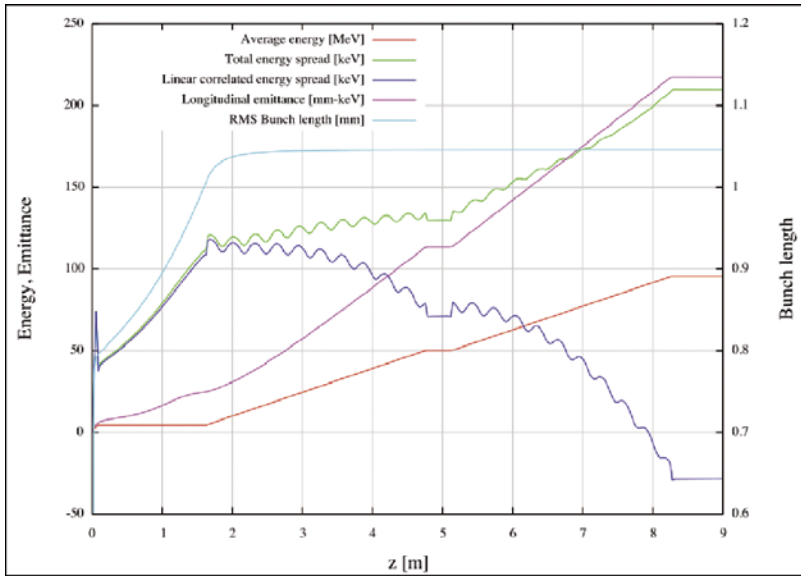


Figure 5.4.7:
Longitudinal beam evolution through the injector.

The linear correlation indicates the orientation of the phase space. It has greatest meaning in the region upstream of the booster linac sections. RF field curvature in the linac introduces significant quadratic and higher order polynomial nonlinearities. The resulting longitudinal phase space of the beam in the gun-to-linac and booster-to-linac regions is shown in Figure 5.4.8.

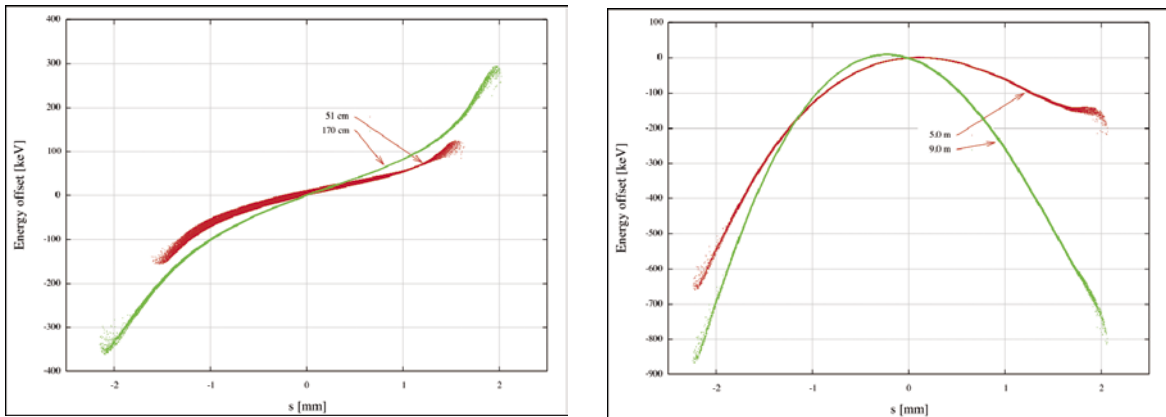


Figure 5.4.8:
Longitudinal phase space in the gun-to-linac region (respectively at 50 cm and at 170 cm from the cathode) (on the left), and at the exit of SØA (at 5 m from the cathode) and SØB (at 9 m from the cathode) (on the right).

In the gun-to-linac region, the overall energy spread is dominated by the correlated contribution. The longitudinal emittance blow-up in the gun-to-linac drift is due to the increase in bunch length and to increasing space charge force terms.

The baseline beam dynamics outlined above was used to generate a collection of nominal beamline parameters that led to optimized RF gun voltages and phases, solenoid magnet peak field settings, booster linac voltages and phases, etc. For each gun mode frequency separation value, a set of beam dynamics simulations was produced, both with and without the zero mode, as a function of the pi-mode phase with respect to the bunch launch time.

The modes are assumed to be excited by the GTF-like klystron pulse described previously, which introduces specific zero-mode amplitudes and phases relative to the pi mode. The zero mode, when present, lags behind in phase with respect to the pi mode according to the phase difference tabulated in Table 5.4.2. This effectively allows studying the beam dynamics sensitivity to the stability of the laser arrival time at the photocathode.

Analysis of the beam transverse phase space at the injector exit (~ 8.28 m) provides information on the degree to which the zero mode excitation interferes with the emittance compensation process. In general, for the relatively long and intense bunches considered here, one finds that the normalized emittance is more sensitive to offsets in the pi-mode phase than to the presence of a perturbing zero-mode. This because space charge forces and 'normal' RF field nonlinearities (due to the pi mode alone) are the dominant contributors to transverse emittance and energy spread. Nevertheless, quantitative understanding of the zero-mode influence will be essential during commissioning and whenever short and/or low charge bunches are used.

5.4.6.1 Transverse Phase Space

The transverse emittance variation with the pi-mode phase is shown in Figure 5.4.9. The quoted bunch emittances are averages over 100 longitudinal bunch slices.

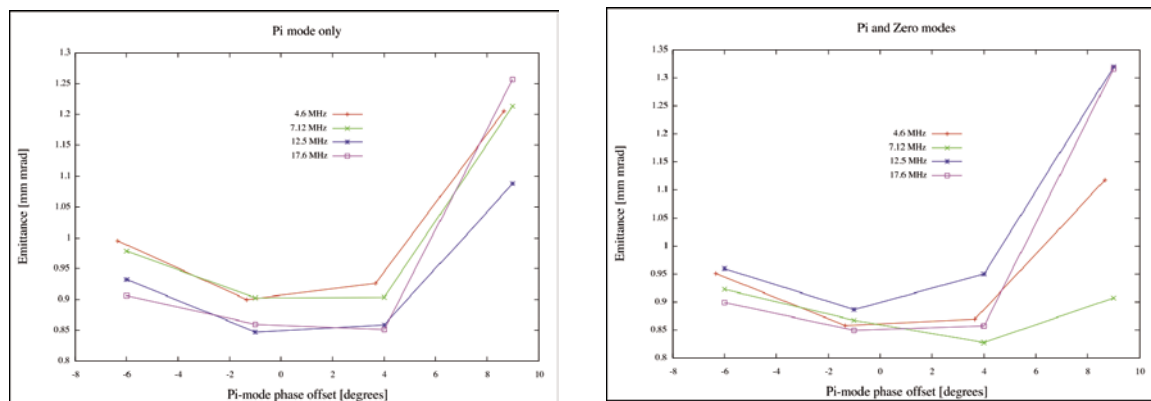


Figure 5.4.9:

Variation of normalized transverse emittance with respect to pi-mode phase offset, for the pi-mode only cases (on the left) and pi+zero-mode cases (on the right).

The emittance sensitivity to phase offsets decreases at negative detuning angles while it increases for positive detuning. When adding the zero mode excitation, the transverse emittance sensitivity to the pi mode phase remains more or less constant, an indication that the zero mode influences primarily the longitudinal phase space. The figure also shows that, as mentioned above, changing the cavity geometry (the beam transit RF phase) in the direction of increasing the mode separation improves the emittance only slightly.

5.4.6.2 Longitudinal Phase Space

The influence of the zero mode on the longitudinal phase space footprint was initially noticed studying the correlated energy spread of photoinjector-generated electron bunches [17]. Beating between the two modes introduces additional correlated energy spread that must be accounted for in following the beam through the accelerator.

Results of beam dynamics simulation runs are compared in the gun-to-linac drift region (~ 0.5 m), before the nonlinear RF curvature makes it difficult to extract the influence of the zero-mode. Differences in total energy spread, linear correlation, and longitudinal emittance between the pi+zero mode cases and the pi-mode only cases, computed as a function of the pi-mode phase offset, are shown in Figure 5.4.10, Figure 5.4.11 and Figure 5.4.12.

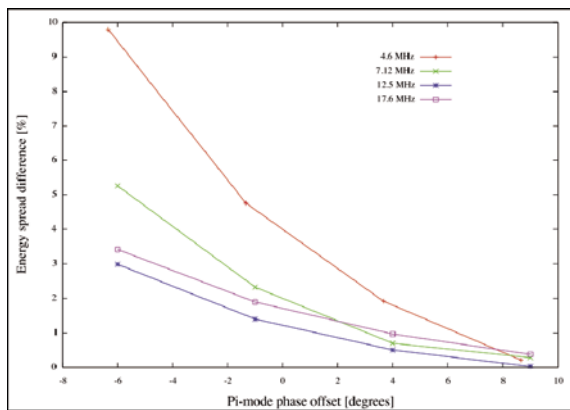


Figure 5.4.10:
Difference in total energy spread between pi+zero mode cases and pi-mode only cases.

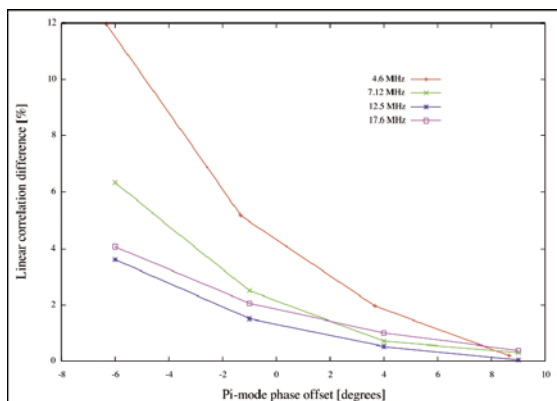


Figure 5.4.11:
Difference in linear correlation between pi+zero mode cases and pi-mode only cases.

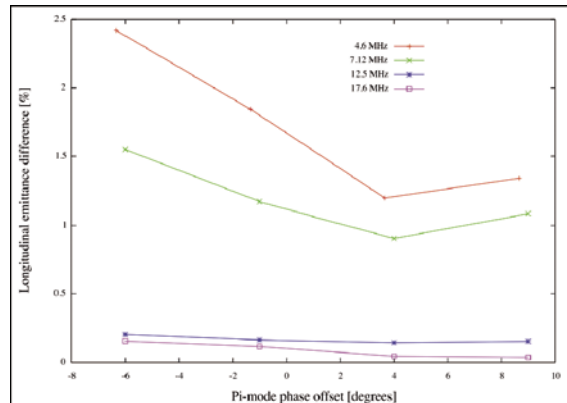


Figure 5.4.12:
Difference in longitudinal emittance between π +zero mode cases and π -mode only cases.

Comparing the results of Figure 5.4.10 and Figure 5.4.11, it is again evident from simulations that in the gun-to-linac drift region the total energy spread is dominated by the correlated one. Several interesting and relevant effects of the zero-mode excitation are observed. First, the difference in the amount of correlated energy spread generally decreases as the mode separation increases. Second, the sensitivity of the difference in the correlated energy spread with respect to the π -mode phase offset significantly decreases as the mode separation increases. Last, the difference in longitudinal emittance (Figure 5.4.12) is largely removed by increasing the mode separation.

5.5 Diagnostic Beamline Design

Figure 5.5.1 shows the photoinjector and diagnostic beamline layouts. The diagnostics in this area monitors the gun performance and characterizes the electron bunch produced by the RF gun. The low

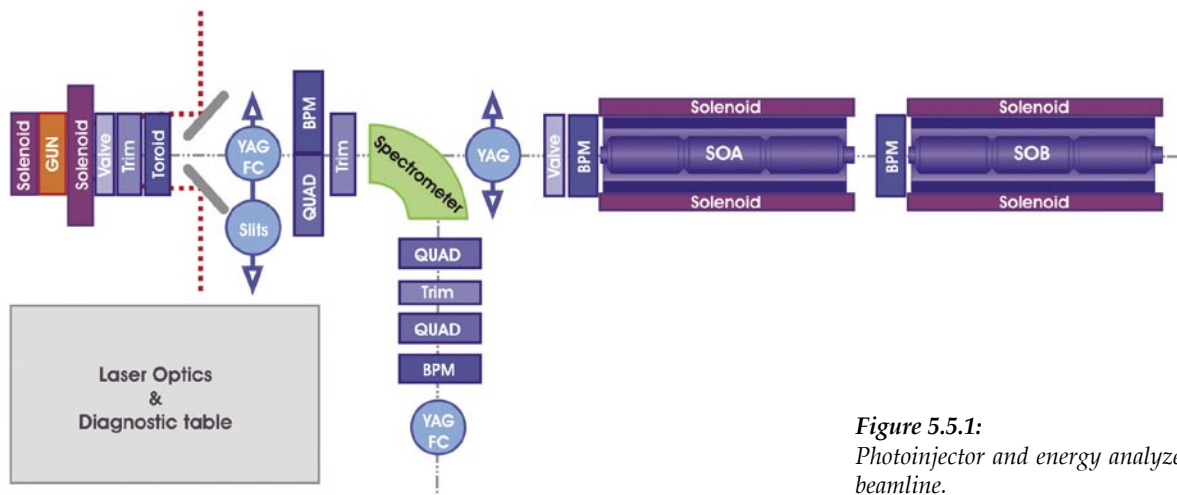


Figure 5.5.1:
Photoinjector and energy analyzer beamline.

energy transport line from the gun to the entrance of the first booster linac (SØA) allows for two modes of operation: direct transport (“in-line”) and deflection to an energy analyzing branch beamline. Two horizontal and vertical dipole correctors (trim) and two BPMs allow for trajectory corrections. A single magnetic quadrupole is included in the direct transport beamline to compensate for any residual phase-induced quadrupole field components in the RF gun or in the linac coupling cells that may interfere with emittance compensation by breaking the cylindrical symmetry. Standard in-line and intercepting diagnostics measure the bunch current, transverse distribution and emittance. An energy analyzer comprised of a 90° bend and three quadrupoles will be used to measure the beam energy and energy spread. A streak camera deployed at the end of the energy analyzer beamline allows for detailed study of the beam longitudinal phase space profile. A complete description of the individual diagnostic components appears in Chapter 11.

5.5.1 RF Gun and In-line Transport Optics

The in-line beamline connects the RF gun output flange to the entrance to the booster accelerator (SØA/SØB) and to the following linac sections. The current physics model of the beamline assumes idealized field profiles of the beamline elements. The electron beam distribution, RF gun and linac cavity modes, solenoid magnet fields, and the resulting beam dynamics were assumed to be axisymmetric. In this approximation, no additional beamline elements are required to generate the high-brightness electron bunches and propagate them between the gun and booster linac.

The physics model uses a simplified, free space model of the solenoid magnets. The resulting field distribution has a fairly long longitudinal reach that may likely interfere with downstream diagnostic performance. A companion bucking solenoid will be included to cancel the on-axis magnetic field at the cathode plane.

5.5.2 Diagnostic Components and Measurements

5.5.2.1 Beam Properties to be Measured Directly

The photoinjector beamline requires diagnostics to accurately and adequately measure the electron beam produced by RF gun and photoinjector laser. Measurements on the electron beam include: (i) bunch charge and photocathode quantum efficiency (Q.E.), (ii) transverse beam position, (iii) beam energy and energy spread, (iv) transverse beam profile, and (v) thermal emittance. Only bunch charge and transverse beam position measurements may be performed with non-interceptive diagnostics. All other measurements will require beam interception and/or deflection. Additional measurements need to be performed on the photoinjector laser beam. Most important are the laser spot size, energy distribution and total energy deposited at the photocathode. They are provided by optical diagnostics (virtual cathode and camera, laser pulse joule-meter, etc.) located close to the RF gun. Information on the longitudinal laser pulse distribution will be obtained from the optical spectrum, and/or by direct measurement with a streak camera.

Beam current and bunch charge will be closely monitored during commissioning and operation to detect and correct any slow drift in the photocathode average quantum efficiency (Q.E.): charge variations will be fed-back to the photocathode drive laser in order to correct them by modulating the laser intensity. A map of the photocathode Q.E. over the region of interest can then be obtained by sweeping a small size laser spot over the cathode and measuring the emitted photo current.

Abnormally large charge variations that could indicate large changes in the average photocathode Q.E. will require more extensive corrective action.

5.5.2.2 Summary of Standard In-Line Diagnostic Elements

The in-line beamline is equipped with a standard complement of diagnostics. Bunch charge will be inferred from current measurements using an inductive toroid and an intercepting Faraday cup (FC). The difference signals from capacitive button-type beam position monitors (BPMs) will provide the bunch charge-centroid position, while the sum signals will be used to measure the bunch charge after calibration with the FC. To determine the photocathode quantum efficiency the drop-in Faraday cup will provide the most accurate bunch charge values.

YAG-coated scintillator screens generating optical transition radiation (OTR) when hit by the beam will be the primary diagnostic for transverse electron beam size and profile. Paired with an upstream quadrupole magnet, they will be used to measure the transverse beam emittance by the quadrupole-scan method. At low bunch charges, the photocathode thermal emittance may also be measured in the same way.

5.5.2.3 Standard Diagnostic Resolution and Sensitivity

The electron beam charge is specified to be in the 0.3-1.0 nC range, with a ~ 10 ps (FWHM) bunch length under normal operation conditions. The charge measurement nominal resolution is consequently specified to be in the ~ 10 -50 pC range. A spot size diameter at the cathode of around 0.5 mm (rms) increases up to 2-3 mm before entering the solenoid at about 30 cm from the cathode. The solenoid focuses the bunch down to 0.4 mm (rms) at about 1.5 m from the cathode. Thus position resolution of ~ 10 -100 μm is sufficient when measuring the transverse bunch size before it enters the solenoid.

During commissioning and for measuring the thermal emittance, the injector may be operated at reduced bunch charge levels, typically ~ 50 pC or less. To measure the charge, Faraday cups with less than 10 pC resolution will have to be deployed on both beamlines. At such low bunch charges the YAG-coated OTR screens have sufficient sensitivity to provide gross spot size and trajectory measurements.

5.5.3 Beam Properties Measured with an Energy Analyzer and Streak Camera

A dispersive beamline that deflects the beam by 90° is used to measure the average beam energy and energy spread. Single-shot streak-camera measurements of Cherenkov or OTR light radiated by the final screen may be used to probe the longitudinal beam distribution and determine the longitudinal phase space emittance.

5.5.3.1 Energy Analyzer Optics

A detailed description of the energy analyzer optics is given in Section 5.4 of Ref. [3]. Its optical functions have been designed to minimize the beam spot size at the image screen, while maintaining a given dispersion. The resulting optical functions are shown in Figure 5.5.2.

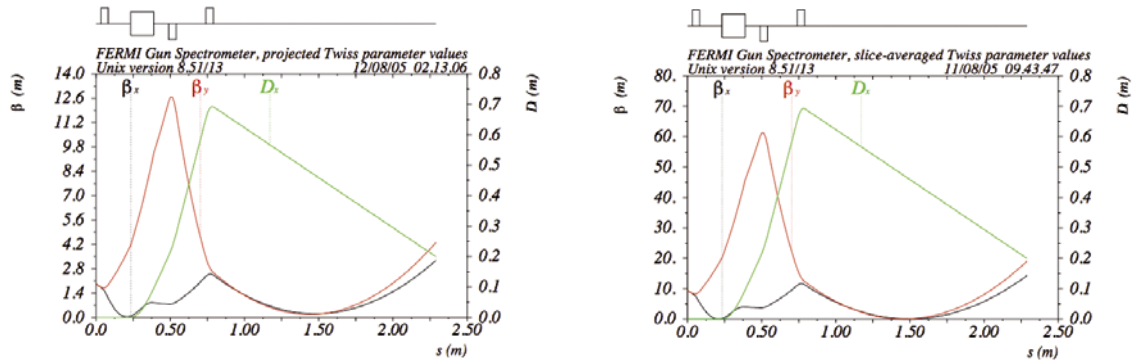


Figure 5.5.2:
MAD models of energy analyzer showing the evolution of projected (left) and slice-averaged (right) Twiss parameters.

The screen location at ~ 1.5 m coincides with the nominal beam waist position. At this point, for a beam energy of 5.3 MeV, or $\gamma \sim 10.4$ the optical functions and the emittance take the values:

$$\begin{aligned} \beta_x &\sim 0.25 \text{ m} \\ D_x &\sim 0.45 \text{ m} \\ \varepsilon_x &\sim (1.0 \text{ mm mrad}) / (10.4) = 0.1 \text{ mm mrad} \end{aligned}$$

The minimum relative energy resolution is then $\delta_{\min} \geq 3.6 \cdot 10^{-4}$, or ~ 2 keV.

The beamline layout presented here is the result of a compromise between the requirements of producing a high brightness electron beam, which tends to require shorter drift lengths between the RF gun and the first booster linac for proper emittance compensation, and the needs of the diagnostics and other instrumentation required to diagnose and to preserve the high quality of the beam.

5.6 Injector Performance Studies

The beam dynamics in the injector system has been modeled extensively - from the photocathode to the exit of the booster accelerator modules - using 2D and 3D space-charge tracking codes (GPT and ASTRA). Some approximations have been made regarding the beamline and its components. Firstly, the entire beamline was assumed to possess perfect azimuthal symmetry about the beamline axis. Secondly, the RF gun model used in the simulations did assume the presence of the TM₀₁₀- π ('pi') mode only. As shown in the previous sections, the lower-frequency mode response is a complicated function of the RF pulse history and gun geometry. The optimization studies presented here will therefore require some recalibration once the RF gun behavior has been more completely characterized. Lastly, longitudinal wakefield effects from the booster accelerator structures have been included in an approximate form: time-dependent longitudinal impulses are computed based on the published wakefield data [18] and the longitudinal bunch charge distribution.

Flexibility in the beamline design and tuning for optimum performance has required some compromise. Space allocation for the beamline instrumentation, including the special diagnostic-dedicated branch requires a minimum drift distance between the RF gun exit and the first booster structure entrance of about 1.6 m, still sufficiently close to the optimum matching point for emittance compensation located at ~ 1.4 m from the cathode.

To optimize the performance in the remainder of the linac, a new type of initial pulse current shape, namely a linear ramped current distribution, has been adopted. In particular, to produce a bunch with uniform current and energy at the entrance of the FEL undulators, accelerating structure wakefields and compression parameters effects lead to the choice of a bunch current in the shape of a quasi-linear head-to-tail ramp. This section describes the optimized beam dynamics for the ramped current distribution for two different bunch configurations: a 0.8 nC/9 ps long “medium length bunch (MLB)” and a 1 nC/11 ps “long bunch (LB)”, and includes parametric sensitivity studies and parameter jitter analysis.

5.6.1 Optimum Baseline Configurations

Table 5.6.1 summarizes the main optimized bunch parameters at the exit of photoinjector, in both the MLB and the LB regimes.

Table 5.6.1: Main bunch parameters at the exit of the photoinjector.

<i>Parameters at the exit of the photoinjector</i>	<i>MLB</i>	<i>LB</i>
Electron beam energy [MeV]	95	95
Bunch charge [pC]	800	1000
Peak current [A]	From 40 to 80	From 40 to 100
Ramped Bunch length [ps]	8	9
Slice emittance [mm-mrad]	< 1	< 1
Projected emittance [mm mrad]	< 1.5	< 1.5
Energy spread (uncorrelated) [keV]	<2	<2

5.6.1.1 Medium Length Bunch Regime

In a seeded FEL, the temporal overlap of an ultra short (~ 100 fs) seed laser pulse with the electron beam at the undulator entrance is a critical issue. To relax jitter tolerances, a ‘medium length’ bunch case has been considered, consisting of a 600 fs electron bunch with a peak current around 1 kA. This translates to a required extracted charge of 800 pC and to a drive laser pulse at the cathode of about 9 ps FWHM, with 0.5 ps of rise/fall time. As mentioned earlier a conservative value of 110 MV/m for the gun accelerating gradient was considered, even if better performances could be obtained by increasing it to 140 MV/m.

As described in [19] a backward tracking simulation performed by LiTrack [20] revealed that a linearly ramped current distribution at the photoinjector exit is a very convenient method to linearize the

wakefields fields in the Linac accelerating sections. Figure 5.6.1 shows the longitudinal phase space (a) and the current profile (b) required by the linac optimization studies at the exit of the photoinjector for the MLB case.

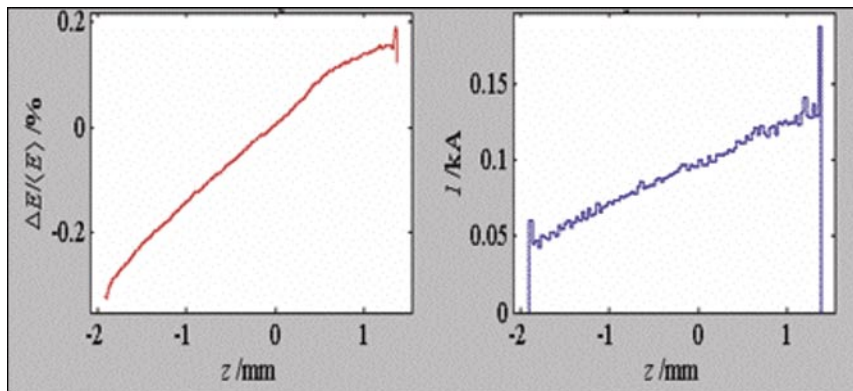


Figure 5.6.1:
On the left: Longitudinal phase space; on the right: current distribution at the exit of the photoinjector for the MLB case (peak slice current on the bunch tail, LiTrack notation).

In order to satisfy these requirements, and to provide an injector output beam with a tailored current profile, the evolution of the initial profile of an emitted bunch in the injector due to the strong non-linearity of the longitudinal space charge field has been studied: the redeal is referred to [21, 22] for a more detailed description. Several initial current distributions were analyzed in order to find the one which best linearizes the space charge field. In order to avoid a strong compression along the linac, the linear current ramp bunch at the injector exit must be about 2.5 mm (~ 8 ps) long. Because the bunch length is blown-up during transport from the cathode to the first accelerating section, the above

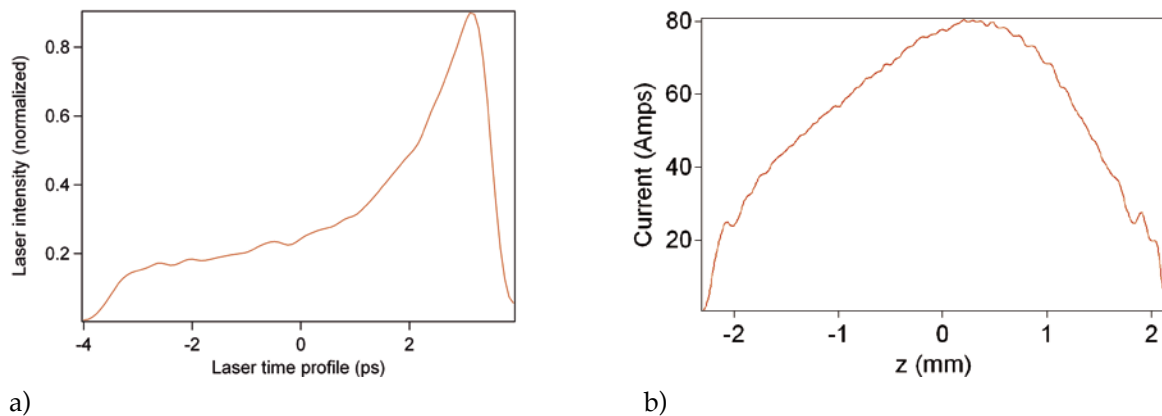


Figure 5.6.2:
a) The optimized longitudinal laser shape is a fourth-degree polynomial;
b) Bunch current distribution at the end of the photoinjector, LiTrack notation.

requirement limits the allowed ramped fraction of the bunch. A fourth-degree polynomial distribution (see Figure 5.6.2) was found to be effective in compensating the high orders contributions of the space charge field (see Figure 5.6.3) while maximizing the bunch fraction that samples a linear space-charge field. The current distribution plotted in Figure 5.6.2a has been adopted as the baseline ramp for the MLB case, with the assumption that the laser pulse can be so shaped. However in a more conservative scenario even a quadratic distribution could be used without severe drawbacks.

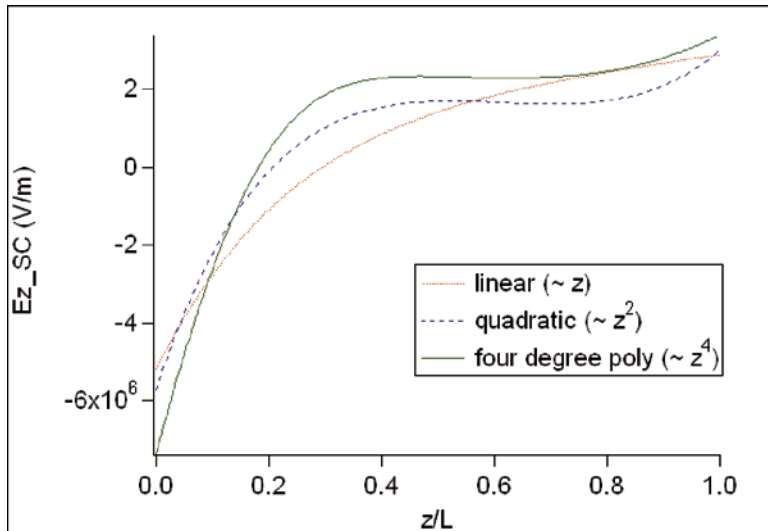


Figure 5.6.3: Comparison between the longitudinal space charge fields sampled by a linear, a quadratic and a fourth-degree polynomial distribution at the cathode.

Because of the non-uniform charge distribution of the ramp, it is difficult to find an injector parameter set that completely satisfies the invariant envelope equation, performing perfect emittance compensation for all slices. Since each slice contains a different amount of charge for any given set of injector parameters, it evolves in a particular and unique way in the gun-to-SØA drift. An “average” setting has therefore been found that minimizes the projected emittance at the exit of the photoinjector (see Figure 5.6.4). The resulting emittance, including the thermal contribution, reaches ~1.39 mm mrad, and if one includes only 80% of the bunch particles, reduces to 1.21 mm mrad.

The thermal emittance contribution has been included following the empirical formula [16]:

$$\varepsilon_{th} (\text{mm mrad}) = 0.16 + 0.93 \cdot \sigma_x (\text{mm}) \quad 5.6.1$$

where σ_x is the drive laser spot rms radius.

Thus, assuming a drive laser spot radius of 1mm, the thermal emittance is about 0.6 mm mrad.

Dividing now the longitudinal bunch profile at the end of SØB into 100 slices and calculating the emittance and the energy spread of each slice, one obtains the plot shown in Figure 5.6.5. As expected, the ramped current distribution also affects the slice emittance modulation along the bunch. The slice emittance of the minimum current slices (at the head) is around 0.7 mm mrad, while the highest current slice reaches 1.1 mm mrad. Figure 5.6.6 shows a top view of the bunch at the injector exit: the transverse dimension is quite constant along ~70% of the bunch length.

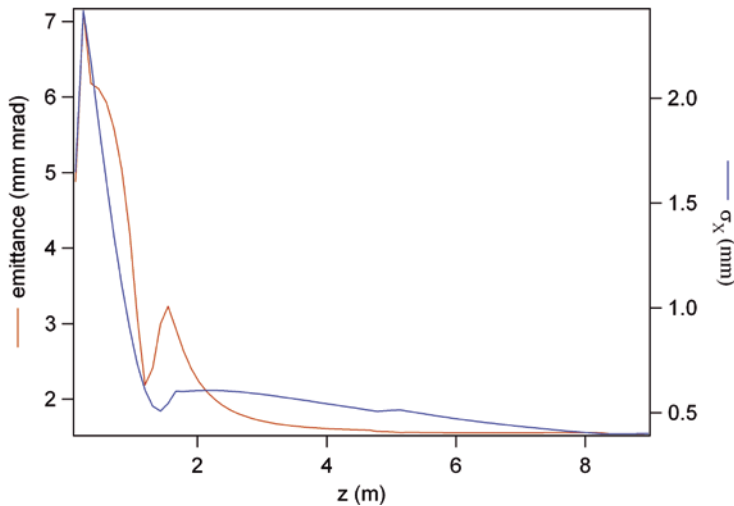


Figure 5.6.4:
Projected Emittance (red line) and RSM transversal spot (blue line) evolution through the injector in the ramped MBL regime.

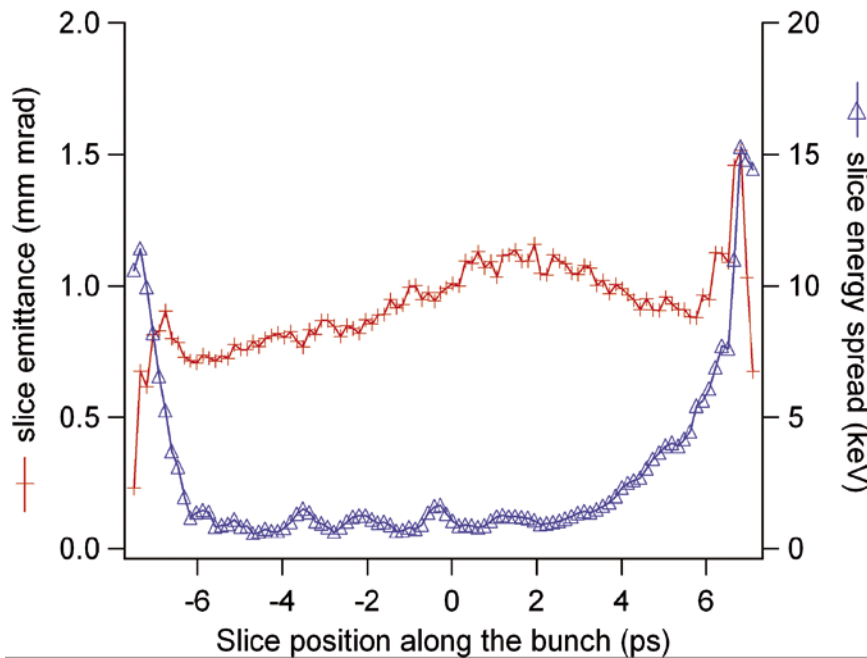


Figure 5.6.5:
Slice emittance (red line) and slice energy spread (blue line) along the ramped MBL bunch, at the exit of the photoinjector (~100 MeV). The head of the bunch is on the left.

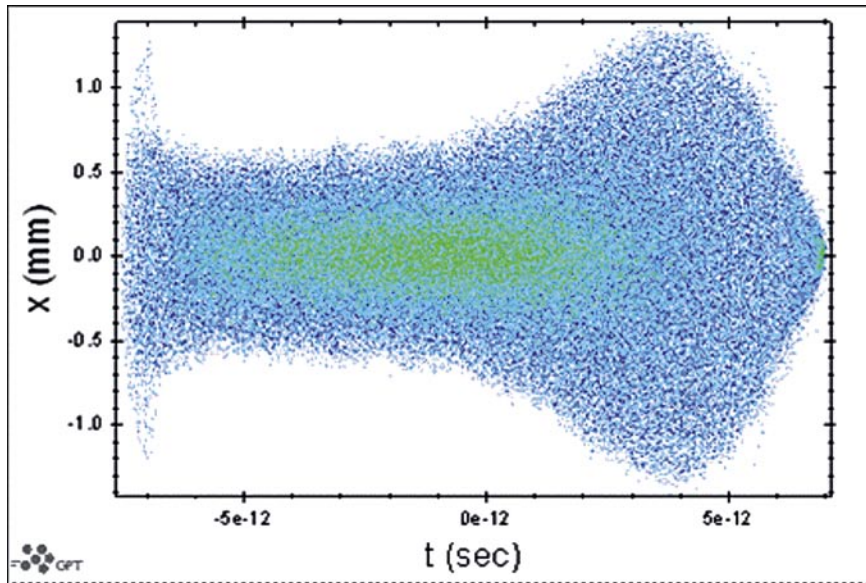


Figure 5.6.6:
Top view of the ramped MBL calculated at the exit of the photoinjector. The head of the bunch is on the left.

5.6.1.2 Long Bunch

The 'long' bunch case is the configuration selected for running at high bunch charge (1 nC) and a long drive laser pulse (~ 10 ps) at the cathode. An in-depth investigation of the best ramped current profile was carried out, starting from the backtracked results obtained with Litrack and plotted in Figure 5.6.7.

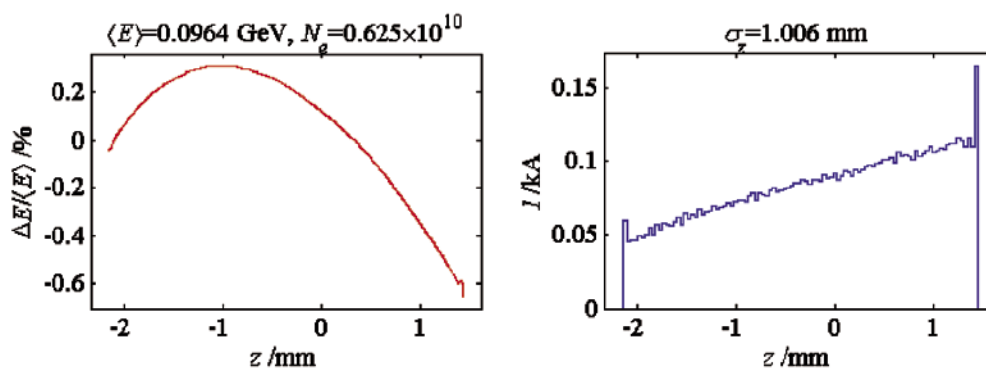


Figure 5.6.7:
(On the left) Longitudinal phase space and (on the right) current distribution at the exit of the photoinjector for the long bunch case (highest slice current in the bunch tail) obtained by the Litrack backtracking.

As in the MBL case, the electrons in the highest current region are pushed back by the space charge forces in the gun-to-SØA drift, so that only a fraction of the bunch has a ramped current profile. It was found that the length of the non-ramped fraction depends mainly on the highest (peak) slice current value, I_{peak} : for $I_{\text{peak}} \sim 100$ Amps, the non-ramped fraction is about 1-1.5mm long. Since in the LB case the required ramp is longer than in the MBL case (~ 4 mm, i.e. ~ 13 ps) the ramped fraction of the bunch at the injector exit must also be longer.

Figure 5.6.8 shows the optimized laser pulse shape at the cathode and the electron bunch current profile at the exit of the photoinjector: the ramped fraction is about 66% of the total.

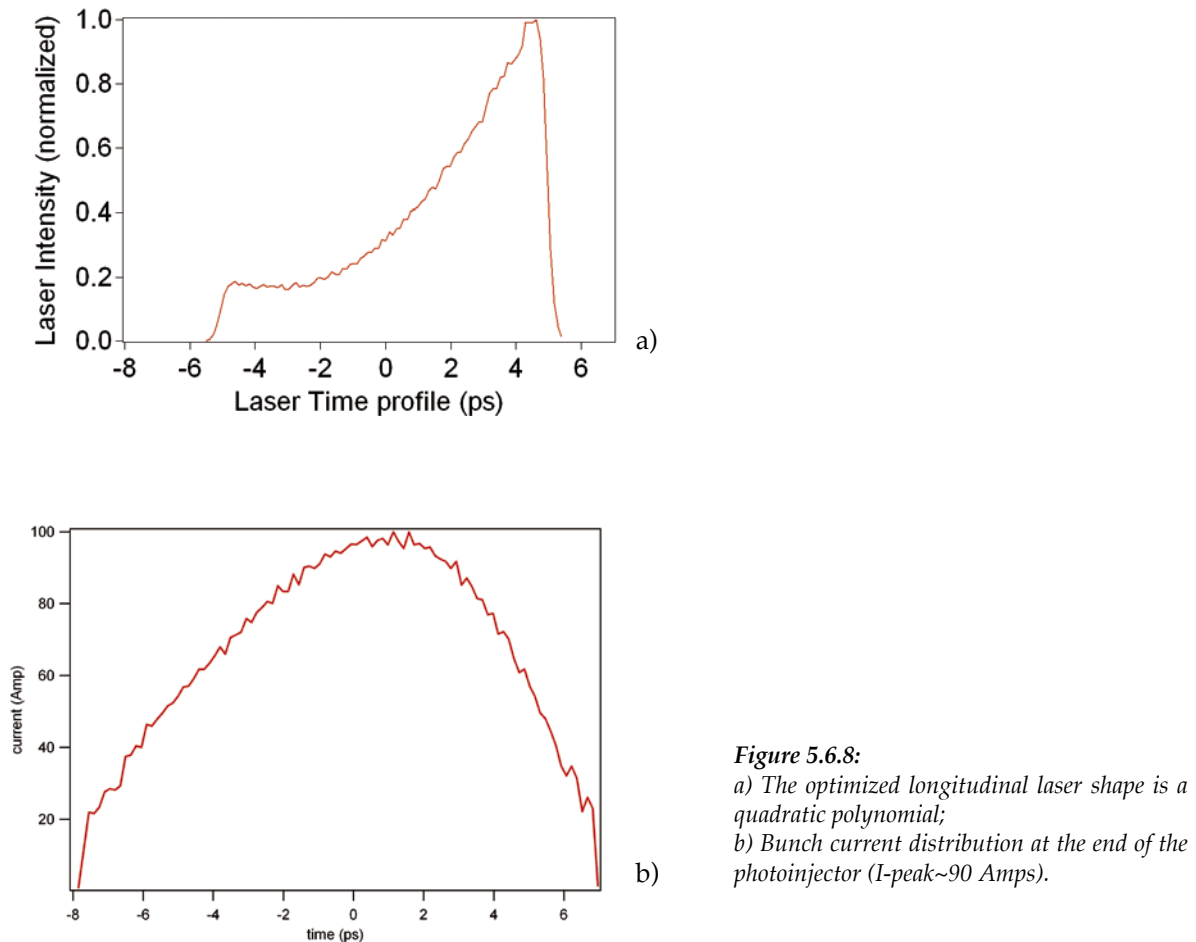


Figure 5.6.8:
 a) The optimized longitudinal laser shape is a quadratic polynomial;
 b) Bunch current distribution at the end of the photoinjector ($I_{\text{peak}} \sim 90$ Amps).

Figure 5.6.9 shows the result of the emittance compensation process. Even in this case, because of the non uniformity of the slice charge density, obtaining good matching condition is an issue. At 100 MeV the projected emittance reaches 1.39 mm mrad.

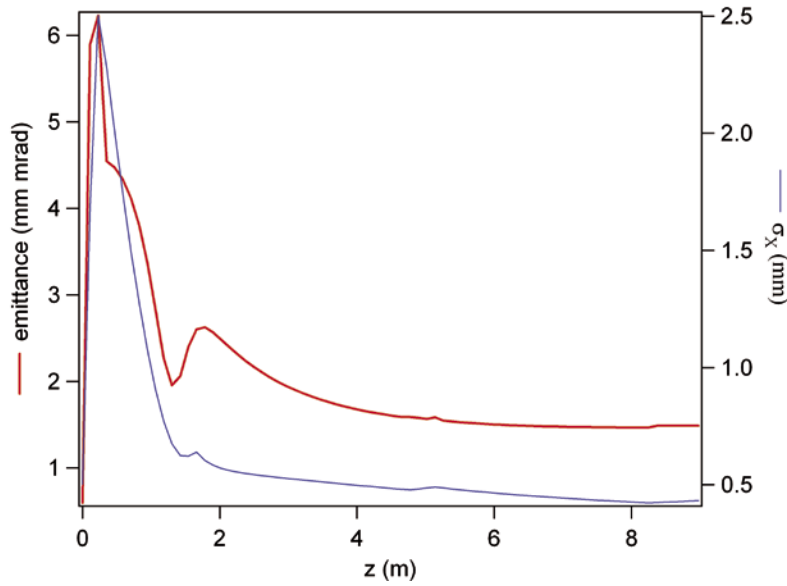


Figure 5.6.9:
Projected Emittance (red line) and rms transversal spot (blue line) evolution through the injector in the ramping long bunch regime.

As in the MBL case a slice analysis of the bunch at the exit of the photoinjector was performed and the results are shown in Figure 5.6.10. The slice emittance behavior (from 0.7 to 1.2 mm mrad) is consistent with the charge density ramp along the bunch and satisfies the specification (less than 1.5 mm mrad).

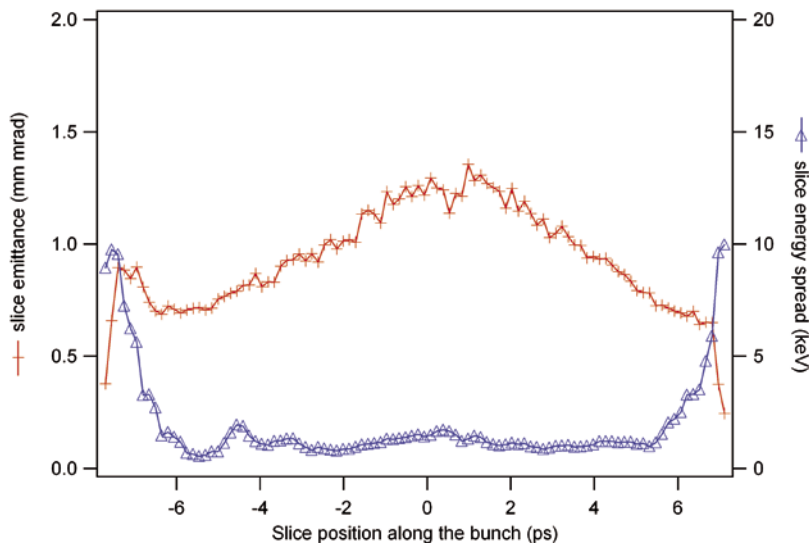


Figure 5.6.10:
Slice emittance and energy spread along the bunch for the LB case.

5.6.2 Parametric Sensitivity Studies

5.6.2.1 Parameter Choices, Tolerances and Jitter Studies

The stability and the robustness of the proposed baseline injector configuration has been investigated. The characteristic variations of the output bunch parameters as a function of the input parameters have to be carefully estimated, because a seed harmonic cascade FEL is very sensitive to shot-to-shot stability. The temporal stability of the electron bunch at the entrance of the undulator, for example, is an important operational requirement to guarantee a reliable synchronization with the seed laser. Moreover the energy stability of the electron bunch is a condition for the stability of the FEL radiation itself; it is therefore important to investigate the contribution to the energy jitter of the injector parameters jitters.

Time of flight, energy, energy spread, peak current and emittance at the end of the injector have been identified as the main output parameters whose shot by shot variation, as well as the corresponding effects on the bunch slice properties, should be quantified.

Moreover, the strong correlation introduced by space charge effects between the various injector parameters does not allow considering each of them separately, but requires performing complete tracking simulations that include all the jitters simultaneously. By randomly sampling each injector component parameter within a tolerance range dictated by present technology, a large number of injector cases have been tracked with GPT and ASTRA, thus obtaining a statistically significant evaluation of the expected jitter of relevant beam output parameters. The solenoid current jitter has been neglected because of the very high stability specified for its power supply. Table 5.6.2 shows the expected rms jitter of each of the considered injector parameters while the computed beam output jitters are collected in Table 5.6.3 and Table 5.6.4.

Table 5.6.2: Expected rms variations of the injector parameters.

<i>InjectorParameter</i>	<i>Expected rms variation</i>
RF injection phase	0.1 deg
Laser Arrival time	200 fs
Gun Eacc	0.25 %
Solenoid strength	0.005 %
SØA-SØB Eacc	0.25 %
SØA-SØB RF phase	0.1 deg
Charge (laser pulse energy)	4 %
Laser spot size	4 %
Laser pulse length	5 %

In order to estimate the current jitter an equivalent current \hat{I} , independent from the longitudinal bunch profile, has been defined as:

$$\hat{I} = \frac{Q}{\sqrt{12}\sigma_t} \quad 5.6.2$$

where Q is the total bunch charge and σ_t is the rms bunch length. This figure of merit represents the peak current of a uniform distribution having σ_t as rms bunch length, but the treatment is general and any other distribution (gaussian, parabolic, quadratic, etc...) can be taken as reference, with \hat{I} the corresponding peak current.

Random gaussian sampling of all the injector parameters according to the tolerances of Table 5.6.2 has been performed for the medium and for the long bunch case.

Figure 5.6.11, Figure 5.6.12 and Figure 5.6.13 show the simulated output parameters jitter and the corresponding histograms for the MLB case.

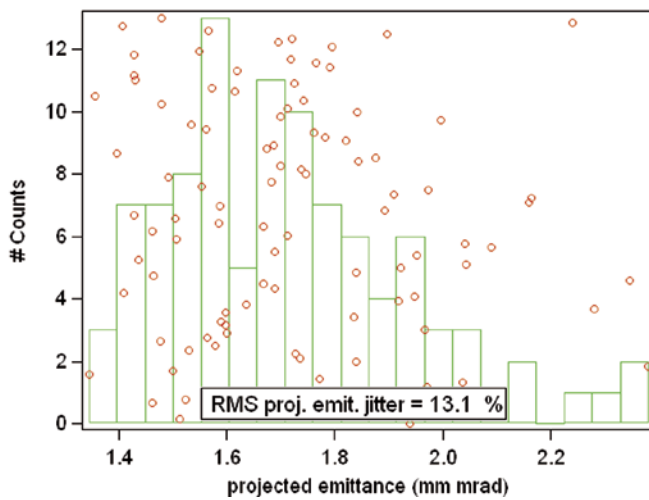


Figure 5.6.11:
Projected emittance jittered values obtained by randomly sampling input injector parameters.

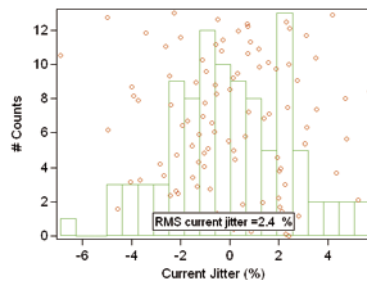
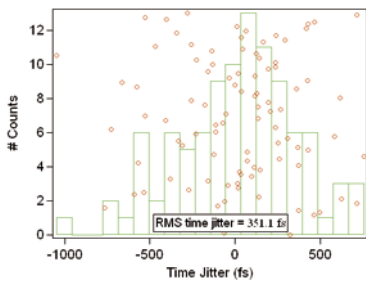


Figure 5.6.12:
Time (on the left) and current (on the right) jittered values obtained by randomly sampling input injector parameters.

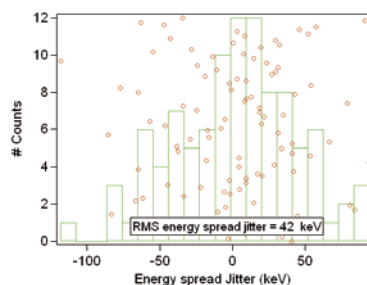
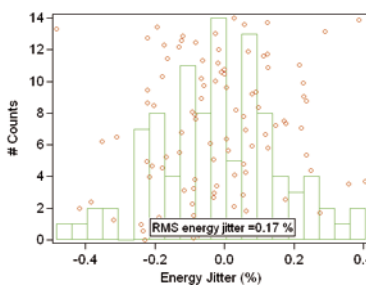


Figure 5.6.13:
Energy (on the left) and energy spread (on the right) jittered values obtained by randomly sampling input injector parameters.

Since the laser pulse shaping process could introduce additional jitter sources, a preliminary study has been made to identify the main parameters whose jitter could affect the shaping of the laser pulse, and their correlation to each other. As an example, a pulse length jitter produces jitter in the ramping current distribution.

Furthermore, regarding the optical matching between the injector and the linac, an analysis of the Twiss parameters jitter has been carried out using the above set of output jittered bunches. The results are given in Table 5.6.3. The average α_x and β_x are respectively -0.09 and 18 m, but the jittered outputs are spread out with a standard deviation of 0.15 and 2.1 m respectively. This should be taken into account for the finalization of the optics matching.

Table 5.6.3: Output parameters jitters for the ramped MLB.

<i>Output parameters</i>	<i>rms jitter</i>
Time (fs)	351
Current (%)	2.4
Energy (%)	0.17
Energy Spread (keV)	42
Emittance (%)	13.1
Alpha	0.15
Beta (m)	2.1

The above described issues concerning the emittance compensation of a ramped current distribution are reflected in a reduced stability of the optimized injector parameters setting, leading to a rms jitter of the projected emittance of about 13%.

As for the MBL case simulations using a set of randomly sampled injector parameters (following Table 5.6.2) were also run. The results are reported in Table 5.6.4.

Table 5.6.4: Output parameters jitters for the long ramped bunch.

<i>Output parameters</i>	<i>rms jitter</i>
Time (fs)	266
Current (%)	3.3
Energy (%)	0.17
Energy Spread (keV)	24
Emittance (%)	6.3
Alpha	0.26
Beta (m)	6.3

5.6.2.2 Sensitivity Studies

The sensitivity of each injector input parameter to time, energy, energy spread, current and emittance jitter has been studied for both the medium length and the long bunch case. In particular, the smallest change of each input parameter with respect to its optimum setting that produces a given change of one of the output parameters was evaluated using ASTRA and GPT. Table 5.6.5 and Table 5.6.6 show the results obtained for the medium length and the long bunch case respectively. As an example, in the medium length bunch case, a 1.5% variation of the gun solenoid field with respect to its optimum value produces a 1% variation of the peak current \hat{I} , while to produce a 100 fs change in the bunch arrival time a 10.7% field increase would be needed.

Table 5.6.5: MBL case. The minimum parameter value variation producing the output variation indicated in brackets in the first row. The range considered to compute the sensitivity is reported in brackets in the first column. (n/s = not sensitive; * = extrapolated).

<i>Parameters (variation)</i>	ΔI (1%)	ΔT (100 fs)	σ_E (10 keV)	$\Delta E/E$ (0.1%)	ϵ_{proj} (10%)	$\langle \epsilon_{slice} \rangle$ 10%
Gun Solenoid (2%)	1.5%	10.7% *	1.1 %	n/s	0.2%	2%
Gun Eacc (1%)	0.47%	0.13%	0.12%	0.96%	0.33%	4.3%
RF phase gun (1°)	0.65° *	2.8°	0.8°	3.8°	0.5° *	4.8° *
SØA Eacc (5%)	20% *	2%	3.9%	0.21%	n/s	n/s
SØA RF phase (0.2°)	6.2° *	n/s	0.1°	1.9° *	n/s	n/s

Table 5.6.6: LB case. The minimum parameter value variation producing the output variation indicated in brackets in the first row. The range considered to compute the sensitivity is reported in brackets in the first column. (n/s = not sensitive; * = extrapolated).

<i>Parameters (variation)</i>	ΔI (1%)	ΔT (100 fs)	σ_E (10 keV)	$\Delta E/E$ (0.1%)	ϵ_{proj} (10%)	$\langle \epsilon_{slice} \rangle$ 10%
Gun Solenoid (2%)	2.2%	10% *	5 % *	n/s	0.8%	1.2%
Gun Eacc (1%)	0.6%	0.15%	0.17%	1.6% *	0.5%	0.9%
RF phase gun (1°)	1.0°	0.3°	0.28°	1.8° *	2.9° *	4.6° *
SØA Eacc (5%)	20% *	2%	1.1%	0.2%	n/s	n/s
SØA RF phase (0.2°)	6.2° *	n/s	0.22° *	0.7° *	n/s	n/s

These results are useful to identify the main sources of output jitter. For example, concerning the time jitter, the main contributions come from the Gun (accelerating gradient and RF phase) and from the time jitter of the laser. The pulse to pulse stability of the ramped current distribution is the object of further studies.

5.6.2.3 Additional Statistical Studies of Bunch Parameters

A polynomial fitting of the longitudinal phase space, current bunch profile and slice emittance provided further insights into the reproducibility of the bunch parameters.

LB case: Figure 5.6.14 shows fourth order polynomial curve fits of the longitudinal phase spaces of twelve randomly selected bunch configurations, while Figure 5.6.15 shows fits of their current profiles. The curves fit the synchronous bunch core (3 mm) with the tails left out.

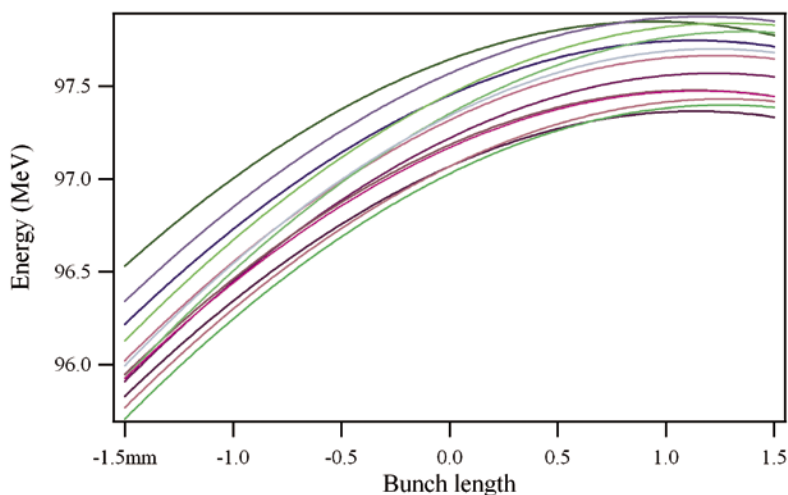


Figure 5.6.14:
12 polynomial curve fits (fourth order), randomly sampled among the thousands performed, of the longitudinal phase spaces of bunches simulated for the long ramped case. Bunch head is on the left.

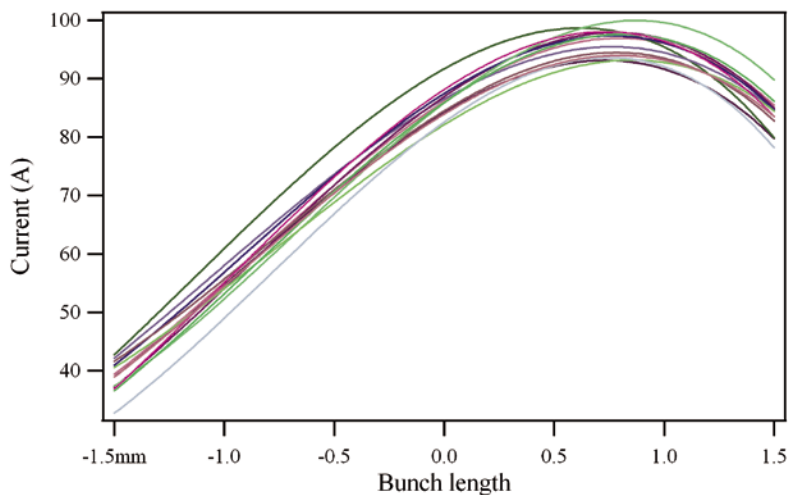


Figure 5.6.15:
12 polynomial curve fits (fourth order), randomly sampled among the thousands performed, of the current profile of bunches simulated for the long ramped case. Bunch head is on the left.

Each fit provides a set of polynomial coefficients for functions described by $f_i(z) = c0_i + c1_i \cdot z + c2_i \cdot z^2 + \dots$ where i is the simulation index. The average coefficient values and their standard deviation (sdv) was computed. Table 5.6.7 reports the results for the longitudinal phase space, the current profile and the slice emittance. The average coefficients can be used to analytically reconstruct the injector output particle distribution including jitter. This knowledge is useful for tracking in longitudinal phase space (for instance using LiTrack).

Table 5.6.7: Statistical analysis of fitting coefficients. The curve function used is a polynomial as: $f_i(z) = c0_i + c1_i \cdot z + c2_i \cdot z^2 + \dots$

<i>Fit coefficient</i>	<i>Longitudinal phase space</i>	<i>Current profile</i>	<i>Slice emittance</i>
<c0>	97.27	86.8	1.06
c0sdv	0.17	3	0.07
<c1>	513	$2.3 \cdot 10^4$	308
c1sdv	50	$2 \cdot 10^3$	45
<c2>	$-2.17 \cdot 10^5$	$-1.14 \cdot 10^7$	$-2.6 \cdot 10^5$
c2sdv	2860	$1.0 \cdot 10^6$	$4 \cdot 10^4$
<c3>	$-6.6 \cdot 10^6$	$-4.0 \cdot 10^9$	$-1.1 \cdot 10^8$
c3sdv	$4.3 \cdot 10^5$	$3.7 \cdot 10^8$	$2 \cdot 10^7$
<c4>	-	-	$5.5 \cdot 10^{10}$
c4sdv	-	-	$9 \cdot 10^9$

5.7 Conclusions

An injector design based on proven technologies and techniques, suitable for producing the high-brightness electron beams required for successful operation of the FERMI@Elettra FELs is presented.

Photocathode performance specifications are well established and conservative. Laser systems are aggressive in average and peak power, but benefit from parallel developments ongoing at other laboratories and in industry. The laser profile tailoring is critical, and will require development to produce suitably reliable pulse shapes at the photocathode.

The design of the off-axis diagnostic beamline in its present stage guarantees that all basic information, such as beam energy, energy spread and position, is obtainable within specification, but still needs additional development and more detailed studies. Additional measurements to be provided for include longitudinal phase space correlations and thermal emittance in the low bunch charge regime.

The sensitivity of the baseline beam dynamics solution to zero mode excitation in the RF gun cavity has been analyzed for various cavity geometries, having different frequency separations between the pi and

the zero mode. An analysis of the transient behavior of the pi and zero modes of the RF gun has been presented. The length and intensity of the electron bunches have been found to affect the longitudinal phase space more than the transverse one. The analysis has also shown heightened sensitivity of the energy correlations present at the RF gun exit to amplitude perturbations resulting from small mode frequency separation.

Optimization of the beamline optics and the drive-laser profile has produced a flexible beamline design that can accommodate various linac operating modes and supply high brightness electron beams suitable for generating a variety of seeded-FEL pulses up to the soft X ray region.

The production and transport of bunches with large initial nonlinear variation of the instantaneous current have been demonstrated to undergo a redistribution of charge such that a linear current ramp is developed over much of the bunch at the injector exit. Such bunches have been shown to be amenable to standard emittance compensation techniques.

The sensitivity of the parameters to changes in some baseline design parameters has been analyzed. The most significant element of the jitter budget remains the timing jitter at the exit of the injector, most of which arises from the drive laser arrival time jitter. For the medium length bunch cases, a rms output timing jitter of ~ 350 fs or less is achievable for a drive-laser arrival time jitter of 200 fs (rms) or less. In the long bunch cases, the tolerances are more relaxed.

5.8 References

- [1] D. Palmer, "The next generation photoinjector", Stanford University dissertation, 1998.
- [2] A. Zholents et al., "Formation of Electron Bunches for Harmonic Cascade X-Ray Free-Electron-Lasers", *Phys. Rev. Spec. Topics Accel. Beams*, **9**, 120701 (2006).
- [3] S. Lidia, G. Penco and M. Trovò, "Technical Design and Optimization Study for the FERMI@Elettra FEL Photoinjector", ST/F-TN-05/13, August 2005.
- [4] K. Flöttman, https://www.desy.de/~mpyflo/Astra_dokumentation.
- [5] S.B. Van der Geer, et. al., <http://www.pulsar.nl/gpt/index.html>.
- [6] A. Zholents et. al., "Formation of electron bunches for harmonic cascade x-ray Free-Electron-Lasers", EPAC'06, Edinburgh, June 2006.
- [7] W. Fawley and G. Penn, "Thoughts on Spectral Broadening Effects in FERMI and other FEL's Based upon Seeded Harmonic Generation", ST/F-TN-06/07, May 2006.
- [8] F.M. Dickey and S.C. Holswade, eds. *Laser Beam Shaping: Theory and Techniques*, Marcel Dekker, Inc. (New York, 2000).
- [9] P. Craievich and V. Verzilov, "Case Study for Modification and Use of the LCLS RF Photoinjector as an Electron Source for the ELETTRA Linac FEL", ST/M-03/02, May 2003.
- [10] T.P. Wrangler, *RF Linear Accelerators*, John Wiley & Sons (1998).
- [11] M. Trovò and P. Craievich, "RF Cavity Geometries for Fermi Gun", ST/F-TN-05/29, December 2005.
- [12] Microwave Studio, CST.
- [13] J. Schmerge (SLAC), private communication.
- [14] J. Schmerge (SLAC), private communication.
- [15] G. Penco, et. al., "Optimization studies of the FERMI@Elettra Photoinjector", Proceedings of the 10th European Particle Accelerator Conference, Edinburgh, 2006.
- [16] W. Graves, et. al., Proceedings of the 2001 Particle Accelerator Conference, Chicago, 2001.
- [17] J. Schmerge, et. al., Proceedings of the Physics and Applications of High Brightness Electron Beams, Erice, 2005.
- [18] P. Craievich, T. Weiland and I. Zagorodnov, "The Short-Range Wakefields in the BTW Accelerating Structure of the ELETTRA Llinac", ST/M-04/02, June 2004.
- [19] A. Zholents et. al., Technical Note, "FERMI@Elettra Accelerator Technical Optimization Final Report", ST/F-TN-06/15, July 2006.
- [20] K. Bane and P. Emma, "LiTrack: a Fast Longitudinal Phase Space Tracking Code with Graphical Interface", PAC '05, Knoxville, Tennessee (2005), 4266.
- [21] G. Penco, "Longitudinal Space Charge Field at the Cathode In Case of a Non Uniform Bunch", ST/F-TN-06/03, March 2006.
- [22] G. Penco, M.Trovò, S.Lidia, "Ramping Longitudinal Distribution Studies for the FERMI@Elettra Injector", Proc. FEL conf. 2006.

Table of Contents

5	Photoinjector	103
5.1	Introduction	104
5.2	Overview of Electron Source and Injection System	104
5.2.1	Electron Source and RF Gun	105
5.2.2	Gun-to-Linac Drift	106
5.2.3	Low Energy Diagnostic Beamline	106
5.2.4	Booster Accelerating Modules	107
5.2.5	Operating Modes	107
5.3	Photocathode and Drive Laser Systems	108
5.4	RF Gun Design and Optimization	109
5.4.1	RF Cavity Design	109
5.4.2	Power Coupling	110
5.4.3	Klystron Pulse Shape and Gun Cavity Transient Response	111
5.4.4	Two-Mode Resonant Cavity Response under Ideal RF Drive	112
5.4.5	Two-Mode Resonant Cavity Response under Measured or Simulated RF Drive	114
5.4.6	Beam Dynamics Simulations	116
5.5	Diagnostic Beamline Design	121
5.5.1	RF Gun and In-line Transport Optics	122
5.5.2	Diagnostic Components and Measurements	122
5.5.3	Beam Properties Measured with an Energy Analyzer and Streak Camera	123
5.6	Injector Performance Studies	124
5.6.1	Optimum Baseline Configurations	125
5.6.2	Parametric Sensitivity Studies	132
5.7	Conclusions	137
5.8	References	139